

Measurement of radiative widths of $a_2(1320)$ and $\pi_2(1670)$

C. Adolph^{8,a}, R. Akhunzyanov^{7,o}, M.G. Alexeev²⁴, G.D. Alexeev^{7,o}, A. Amoroso^{27,28}, V. Andrieux^{22,b}, V. Anosov^{7,o}, A. Austregesilo^{10,17,a,n}, B. Badelek^{31,r}, F. Balestra^{27,28}, J. Barth^{4,a}, G. Baum^{1,a}, R. Beck^{3,a}, Y. Bedfer^{22,b}, A. Berlin^{2,a,b}, J. Bernhard^{13,a}, K. Bicker^{10,17,a,n}, J. Bieling^{4,a}, R. Birsa²⁴, J. Bisplinghoff^{3,a}, M. Bodlak^{19,1}, M. Boer^{22,b}, P. Bordalo^{12,c,m}, F. Bradamante^{25,10}, C. Braun^{8,a}, A. Bressan^{25,24,d}, M. Büchele^{9,a,b}, E. Burtin^{22,b}, L. Capozza^{22,b}, M. Chiosso^{27,28}, S.U. Chung^{17,e,a,n}, A. Cicuttin^{26,24}, M.L. Crespo^{26,24}, Q. Curiel^{22,b}, S. Dalla Torre²⁴, S.S. Dasgupta^{6,k}, S. Dasgupta²⁴, O.Yu. Denisov²⁸, S.V. Donskov²¹, N. Doshita^{33,p}, V. Duic²⁵, W. Dünnweber^{16,a,n}, M. Dziejewicki^{32,r}, A. Efremov^{7,o}, C. Elia^{25,24}, P.D. Eversheim^{3,a}, W. Eyrich^{8,a}, M. Faessler^{16,a,n}, A. Ferrero^{22,b}, A. Filin²¹, M. Finger^{19,1}, M. Finger jr.^{19,1}, H. Fischer^{9,a,b}, C. Franco^{12,m}, N. du Fresne von Hohenesche^{13,10,a}, J.M. Friedrich^{17,a,d,n}, V. Frolov¹⁰, F. Gautheron^{2,a,b}, O.P. Gavrichtchouk^{7,o}, S. Gerassimov^{15,17,a,n}, R. Geyer^{16,a,n}, I. Gnesi^{27,28}, B. Gobbo²⁴, S. Goertz^{4,a}, M. Gorzellik^{9,a,b}, S. Grabmüller^{17,a,n}, A. Grasso^{27,28}, B. Grube^{17,a,n}, A. Guskov^{7,o}, T. Guthörl^{9,f,a,b}, F. Haas^{17,a,n}, D. von Harrach^{13,a}, D. Hahne^{4,a}, R. Hashimoto^{33,p}, F.H. Heinsius^{9,a,b}, F. Herrmann^{9,a,b}, F. Hinterberger^{3,a}, Ch. Höppner^{17,a,n}, N. Horikawa^{18,g,p}, N. d'Hose^{22,b}, S. Huber^{17,a,n}, S. Ishimoto^{33,h,p}, A. Ivanov^{7,o}, Yu. Ivanshin^{7,o}, T. Iwata^{33,p}, R. Jahn^{3,a}, V. Jary^{20,1}, P. Jasinski^{13,a}, P. Jörg^{9,a,b}, R. Joosten^{3,a}, E. Kabuß^{13,a}, B. Ketzer^{17,a,n}, G.V. Khaustov²¹, Yu.A. Khokhlov^{21,i}, Yu. Kisselev^{7,o}, F. Klein^{4,a}, K. Klimaszewski^{30,r}, J.H. Koivuniemi^{2,a,b}, V.N. Kolosov²¹, K. Kondo^{33,p}, K. Königsmann^{9,a,b}, I. Konorov^{15,17,a,n}, V.F. Konstantinov²¹, A.M. Kotzinian^{27,28}, O. Kouznetsov^{7,o}, Z. Kral^{20,1}, M. Krämer^{17,a,n}, Z.V. Kroumchtein^{7,o}, N. Kuchinski^{7,o}, F. Kunne^{22,b,d}, K. Kurek^{30,r}, R.P. Kurjata^{32,r}, A.A. Lednev²¹, A. Lehmann^{8,a}, S. Levorato²⁴, A. Maggiora²⁸, A. Magnon^{22,b}, N. Makke^{25,24}, G.K. Mallot¹⁰, C. Marchand^{22,b}, A. Martin^{25,24}, J. Marzec^{32,r}, J. Matousek^{19,1}, H. Matsuda^{33,p}, G. Meshcheryakov^{7,o}, W. Meyer^{2,a,b}, T. Michigami^{33,p}, Yu.V. Mikhailov²¹, Y. Miyachi^{33,p}, A. Nagaytsev^{7,o}, T. Nagel^{17,a,n}, F. Nerling^{13,a,b}, S. Neubert^{17,a,n}, D. Neyret^{22,b}, V.I. Nikolaenko²¹, J. Novy^{20,1}, W.-D. Nowak^{9,a,b}, A.S. Nunes^{12,m}, I. Orlov^{7,o}, A.G. Olshevsky^{7,o}, M. Ostrick^{13,a}, R. Panknin^{4,a}, D. Panzieri^{29,28}, B. Parsamyan^{27,28}, S. Paul^{17,a,n}, M. Pesek^{19,1}, S. Platchkov^{22,b}, J. Pochodzalla^{13,a}, V.A. Polyakov²¹, J. Pretz^{4,j,a}, M. Quaresima^{12,m}, C. Quintans^{12,m}, S. Ramos^{12,c,m}, G. Reicherz^{2,a,b}, E. Rocco¹⁰, A. Rychter^{32,r}, N.S. Rossiyskaya^{7,o}, D.I. Ryabchikov²¹, V.D. Samoylenko²¹, A. Sandacz^{30,r}, S. Sarkar^{6,k}, I.A. Savin^{7,o}, G. Sbrizzai^{25,24}, P. Schiavon^{25,24}, C. Schill^{9,a,b}, T. Schlüter^{16,a,n}, A. Schmidt^{8,a}, K. Schmidt^{9,f,a,b}, H. Schmieden^{4,a}, K. Schönning¹⁰, S. Schopferer^{9,a,b}, M. Schott¹⁰, O.Yu. Shevchenko^{7,o}, L. Silva^{12,m}, L. Sinha^{6,k}, S. Sirtl^{9,a,b}, M. Slunicka^{7,o}, S. Sosio^{27,28}, F. Sozzi²⁴, A. Srnka^{5,1}, L. Steiger²⁴, M. Stolarski^{12,m}, M. Sulc^{11,1}, R. Sulej^{30,r}, H. Suzuki^{33,g,p}, A. Szabelski^{30,r}, T. Szameitat^{9,f,a,b}, S. Takekawa²⁸, J. ter Wolbeek^{9,f,a,b}, S. Tessaro²⁴, F. Tessarotto²⁴, F. Thibaud^{22,b}, S. Uhl^{17,a,n}, I. Uman^{16,n}, M. Vandenbroucke^{22,b}, M. Virius^{20,1}, J. Vondra^{20,1}, L. Wang^{2,a,b}, T. Weisrock^{13,a}, M. Wilfert^{13,a}, R. Windmolders^{4,a}, H. Wollny^{22,b}, K. Zarembo^{32,r}, M. Zavertyaev¹⁵, E. Zemlyanichkina^{7,o}, T. Matsuda^{14,p}, J. Lichtenstadt^{23,q}, P. Sznajder^{30,r}, and M. Ziembicki^{32,r}

¹ Universität Bielefeld, Fakultät für Physik, 33501 Bielefeld, Germany

² Universität Bochum, Institut für Experimentalphysik, 44780 Bochum, Germany

³ Universität Bonn, Helmholtz-Institut für Strahlen- und Kernphysik, 53115 Bonn, Germany

⁴ Universität Bonn, Physikalisches Institut, 53115 Bonn, Germany

⁵ Institute of Scientific Instruments, AS CR, 61264 Brno, Czech Republic

⁶ Matrivani Institute of Experimental Research & Education, Calcutta-700 030, India

⁷ Joint Institute for Nuclear Research, 141980 Dubna, Moscow region, Russia

⁸ Universität Erlangen-Nürnberg, Physikalisches Institut, 91054 Erlangen, Germany

⁹ Universität Freiburg, Physikalisches Institut, 79104 Freiburg, Germany

¹⁰ CERN, 1211 Geneva 23, Switzerland

¹¹ Technical University in Liberec, 46117 Liberec, Czech Republic

¹² LIP, 1000-149 Lisbon, Portugal

¹³ Universität Mainz, Institut für Kernphysik, 55099 Mainz, Germany

¹⁴ University of Miyazaki, Miyazaki 889-2192, Japan

¹⁵ Lebedev Physical Institute, 119991 Moscow, Russia

¹⁶ Ludwig-Maximilians-Universität München, Department für Physik, 80799 Munich, Germany

- ¹⁷ Technische Universität München, Physik Department, 85748 Garching, Germany
¹⁸ Nagoya University, 464 Nagoya, Japan
¹⁹ Charles University in Prague, Faculty of Mathematics and Physics, 18000 Prague, Czech Republic
²⁰ Czech Technical University in Prague, 16636 Prague, Czech Republic
²¹ State Scientific Center Institute for High Energy Physics of National Research Center “Kurchatov Institute”, 142281 Protvino, Russia
²² CEA IRFU/SPhN Saclay, 91191 Gif-sur-Yvette, France
²³ Tel Aviv University, School of Physics and Astronomy, 69978 Tel Aviv, Israel
²⁴ Trieste Section of INFN, 34127 Trieste, Italy
²⁵ University of Trieste, Department of Physics, 34127 Trieste, Italy
²⁶ Abdus Salam ICTP, 34151 Trieste, Italy
²⁷ University of Turin, Department of Physics, 10125 Turin, Italy
²⁸ Torino Section of INFN, 10125 Turin, Italy
²⁹ University of Eastern Piedmont, 15100 Alessandria, Italy
³⁰ National Centre for Nuclear Research, 00-681 Warsaw, Poland
³¹ University of Warsaw, Faculty of Physics, 00-681 Warsaw, Poland
³² Warsaw University of Technology, Institute of Radioelectronics, 00-665 Warsaw, Poland
³³ Yamagata University, Yamagata, 992-8510 Japan

Received: 13 March 2014

Published online: 25 April 2014 – © Società Italiana di Fisica / Springer-Verlag 2014

Communicated by H. Ströher

Abstract. The COMPASS Collaboration at CERN has investigated the reaction $\pi^- \gamma \rightarrow \pi^- \pi^- \pi^+$ embedded in the Primakoff reaction of 190 GeV pions scattering in the Coulomb field of a lead target, $\pi^- \text{Pb} \rightarrow \pi^- \pi^- \pi^+ \text{Pb}$. Exchange of quasi-real photons is selected by isolating the sharp Coulomb peak observed at momentum transfer below $0.001 (\text{GeV}/c)^2$. Using a partial-wave analysis the amplitudes and relative phases of the $a_2(1320)$ and $\pi_2(1670)$ mesons have been extracted, and the Coulomb and the diffractive contributions have been disentangled. Measuring absolute production cross sections we have determined the radiative width of the $a_2(1320)$ to be $\Gamma_0(a_2(1320) \rightarrow \pi\gamma) = (358 \pm 6_{\text{stat}} \pm 42_{\text{syst}}) \text{keV}$. As the first measurement, $\Gamma_0(\pi_2(1670) \rightarrow \pi\gamma) = (181 \pm 11_{\text{stat}} \pm 27_{\text{syst}}) \text{keV} \cdot (\text{BR}_{f_2\pi}^{\text{PDG}}/\text{BR}_{f_2\pi})$ is obtained for the radiative width of the $\pi_2(1670)$, where in this analysis the branching ratio $\text{BR}_{f_2\pi}^{\text{PDG}} = 0.56$ has been used. We compare these values to previous measurements and theoretical predictions.

^a Supported by the German Bundesministerium für Bildung und Forschung.

^b Supported by EU FP7 (HadronPhysics3, Grant Agreement number 283286).

^c Also at: Instituto Superior Técnico, Universidade de Lisboa, Lisbon, Portugal.

^d e-mail: Andrea.Bressan@cern.ch; e-mail: jan@tum.de; e-mail: Fabienne.Kunne@cern.ch (Corresponding authors)

^e Also at: Department of Physics, Pusan National University, Busan 609-735, Republic of Korea and at Physics Department, Brookhaven National Laboratory, Upton, NY 11973, USA.

^f Supported by the DFG Research Training Group Programme 1102 “Physics at Hadron Accelerators”.

^g Also at: Chubu University, Kasugai, Aichi, 487-8501 Japan.

^h Also at: KEK, 1-1 Oho, Tsukuba, Ibaraki, 305-0801 Japan.

ⁱ Also at: Moscow Institute of Physics and Technology, Moscow Region, 141700, Russia.

^j Present address: RWTH Aachen University, III. Physikalisches Institut, 52056 Aachen, Germany.

^k Supported by SAIL (CSR), Govt. of India.

^l Supported by Czech Republic MEYS Grants ME492 and LA242.

^m Supported by the Portuguese FCT - Fundação para a Ciência e Tecnologia, COMPETE and QREN, Grants CERN/FP/109323/2009, CERN/FP/116376/2010 and CERN /FP/123600/2011.

ⁿ Supported by the DFG cluster of excellence “Origin and Structure of the Universe” (www.universe-cluster.de).

^o Supported by CERN-RFBR Grants 08-02-91009 and 12-02-91500.

^p Supported by the MEXT and the JSPS under the Grants No. 18002006, No. 20540299 and No. 18540281; Daiko Foundation and Yamada Foundation.

^q Supported by the Israel Science Foundation, founded by the Israel Academy of Sciences and Humanities.

^r Supported by the Polish NCN Grant DEC-2011/01/M/ ST2/02350.

1 Introduction

Radiative decays of mesons are an important tool for the investigation of their internal structure as the electromagnetic transition operators are well known and probe the difference between the initial- and final-state mesons in terms of their electric charge or magnetic current distributions. The established $a_2(1320) \rightarrow \pi\gamma$ decay constitutes a magnetic quadrupole transition. The $\pi_2(1670) \rightarrow \pi\gamma$ decay was not measured before. It represents an electric quadrupole transition, which is expected to probe the charge distribution of the orbitally excited meson out to large distances. Radiative transitions can be calculated using the meson wave function obtained in various quark models. In addition, the vector meson dominance model is used to relate $\rho\pi$ and $\gamma\pi$ decays via the $\rho-\gamma$ equivalence. Various calculations do exist for the radiative width of the $a_2(1320)$. Applying vector meson dominance, a width of 375 ± 50 keV was calculated by ref. [1]. Using a relativistic quark model for the meson wave function, a value of 324 keV was extracted [2], and 235 keV was derived from a covariant oscillator quark model [3]. Newer calculations in this model framework yield 237 keV [4]. The covariant oscillator quark model was also used for a prediction of the radiative width of the $\pi_2(1670)$; for two different model versions values of 335 keV and 521 keV are given in ref. [4].

The direct measurement of electromagnetic couplings using radiative decays of mesons is difficult, as the corresponding branching ratios are small, and background from processes containing $\pi^0 \rightarrow \gamma\gamma$ or $\eta \rightarrow \gamma\gamma$ with one or more of the photons lost may be significant. An alternative access to the radiative transition amplitudes is given by $\pi\gamma$ scattering as provided by Primakoff production of the resonances under investigation, where an ultra-relativistic (*i.e.* quasi-stable) pion beam scatters off the quasi-real photons of the electromagnetic field of a heavy nucleus. The respective flux is given by the Weizsäcker-Williams equivalent-photon approximation [5], which relates the experimentally observed cross section $\sigma_{\pi A}$ to the cross section of real photon scattering $\sigma_{\pi\gamma}$ as

$$\frac{d\sigma_{\pi A}}{ds dt' d\Phi} = \frac{\alpha Z^2}{\pi(s - m_\pi^2)} F_{\text{eff}}^2(t') \frac{t'}{(t' + t_{\text{min}})^2} \frac{d\sigma_{\pi\gamma}(s)}{d\Phi}. \quad (1)$$

The positive quantity $t' = |t| - t_{\text{min}}$ contains the four-momentum transfer squared $t = (p_\pi - p_X)^2$ and $t_{\text{min}} = [(s - m_\pi^2)/2E_{\text{beam}}]^2$ with $m = m_X = \sqrt{s}$ being the invariant mass of a final state X given by $s = (p_\pi + p_\gamma)^2$. The symbol $d\Phi$ denotes the phase-space element as given in ref. [6], eq. (43.11), and Z is the charge of the nucleus with mass number A .

We approximate the form factor $F_{\text{eff}}^2(t')$ by means of the sharp-radius approach of refs. [7, 8] and [9], thus taking into account the distortion of the pionic wave functions in the Coulomb field. We use $|F_C^u(t', t_{\text{min}})|^2$ given in eq. (27) of refs. [7, 8], which also includes the Weizsäcker-Williams term $t'/(t' + t_{\text{min}})^2$. For the extended charge distribution of the lead nucleus, we take a sharp radius of $r_u = 6.52$ fm.

The cross section for the production and decay of a broad resonance X with spin J and nominal mass m_0 , averaged over its spin projections, is parameterised by a relativistic Breit-Wigner function. Modified for the case of pion-induced Primakoff production, it reads

$$\begin{aligned} \frac{d\sigma}{dm dt'} &= 16\alpha Z^2 (2J+1) \left(\frac{m}{m^2 - m_\pi^2} \right)^3 \\ &\times \frac{m_0^2 \Gamma_{\pi\gamma}(m) \Gamma_{\text{final}}(m)}{(m^2 - m_0^2)^2 + m_0^2 \Gamma_{\text{total}}^2(m)} \\ &\times \frac{t'}{(t' + t_{\text{min}})^2} F_{\text{eff}}^2(t'). \end{aligned} \quad (2)$$

Here, $\Gamma_{\pi\gamma}(m) = f_{\pi\gamma}^{\text{dyn}}(m) \Gamma_0(X \rightarrow \pi\gamma)$ is the mass-dependent radiative width with $f_{\pi\gamma}^{\text{dyn}}$ the kinematic factor discussed in sect. 3.1 multiplied by the nominal radiative width $\Gamma_0(X \rightarrow \pi\gamma)$ that is the subject of this paper. The symbol $\Gamma_{\text{total}}(m)$ denotes the total mass-dependent width of the resonance X (see eq. (11) below), and $\Gamma_{\text{final}}(m)$ its mass-dependent partial width for the decay into the investigated final state

$$\Gamma_{\text{final}}(m) = f_{\text{final}}^{\text{dyn}}(m) \Gamma_0(m_0) \text{ CG BR}, \quad (3)$$

where CG is the relevant squared isospin Clebsch-Gordan coefficient of the resonance decay into the investigated final state with branching ratio BR and $\Gamma_0(m_0)$ is the nominal width of the resonance at its nominal mass.

Integrating eq. (2) over the relevant ranges in m and t' , the radiative width is found to be related to the absolute cross section $\sigma_{\text{Primakoff}, X}$ via a constant C_X that is calculated according to eq. (14):

$$\begin{aligned} \sigma_{\text{Primakoff}, X} &= \int_{m_1}^{m_2} \int_0^{t'_{\text{max}}} \frac{d\sigma}{dm dt'} dt' dm \\ &= \Gamma_0(X \rightarrow \pi\gamma) C_X. \end{aligned} \quad (4)$$

Thus the radiative width $\Gamma_0(X \rightarrow \pi\gamma)$ can be determined from the number of events $N_{X, \text{prim}}$ experimentally observed from Primakoff production,

$$\Gamma_0(X \rightarrow \pi\gamma) = \frac{N_{X, \text{prim}} / \epsilon_X}{C_X L \text{ CG BR } \epsilon_{\text{resol}}}, \quad (5)$$

with ϵ_X being the acceptance of the experimental apparatus and the event selection procedure, and L the integrated luminosity corresponding to the analysed data set. Effects due to the finite resolution in t' are absorbed by ϵ_{resol} , which reflects the migration of events from the sharp peak near $t' \approx 0$ to higher values outside of our selected t' region.

2 Primakoff production of resonances in the $\pi^- \pi^- \pi^+$ final state

The COMPASS experiment located at the CERN Super Proton Synchrotron features a large-acceptance and high-precision spectrometer [10]. It offers very good conditions

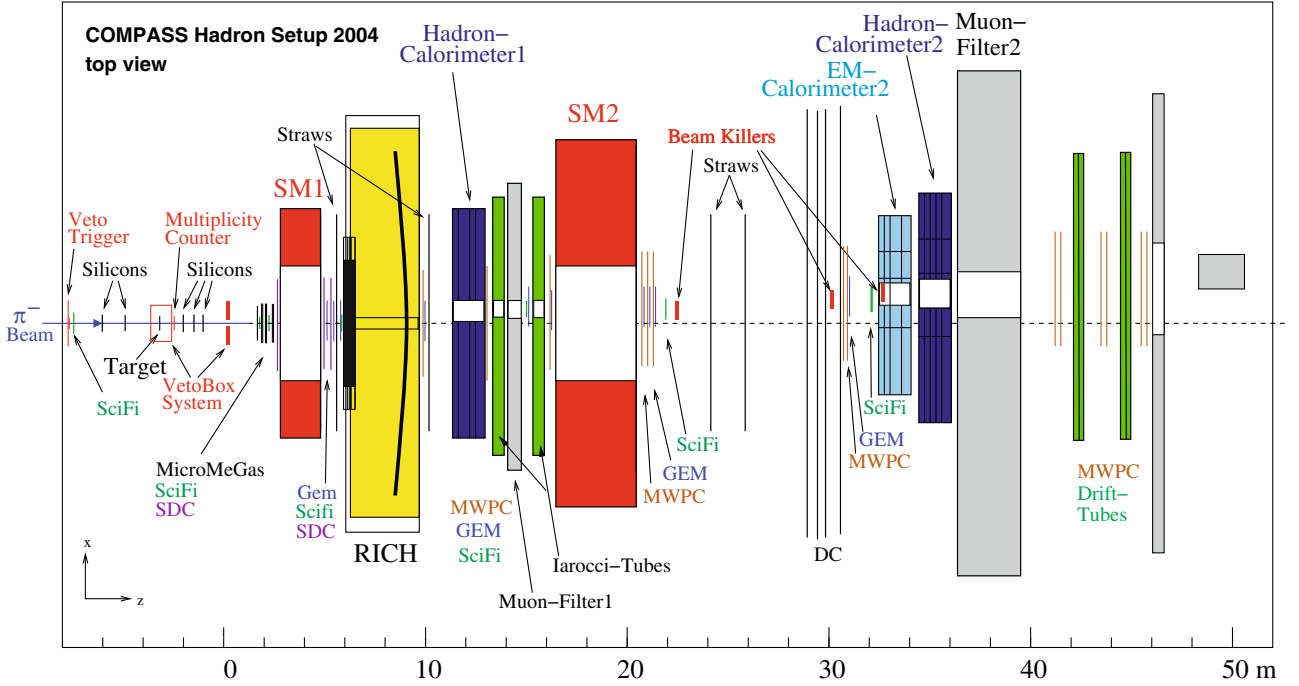


Fig. 1. Sketch of the experimental setup of the Hadron Run in the year 2004.

to study reactions of high-energy beam particles impinging on fixed targets at low-to-intermediate momentum transfers. Its acceptance covers mostly the phase space for final-state particles emerging in forward direction. The data presented in the following were recorded in 2004 using a 190 GeV negative hadron beam, which consists of 96.8% π^- , 2.4% K^- , and 0.8% \bar{p} at the COMPASS target. The experimental setup is sketched in fig. 1. The target is surrounded by a veto system designed to reject non-exclusive forward or large-angle reactions. High-precision silicon micro-strip detectors with a spatial resolution of 8–11 μm make vertex reconstruction possible for smallest scattering angles. The two spectrometer stages, which are arranged around the magnets SM1 and SM2, are both equipped with a variety of detectors for tracking, calorimetry and particle identification. The target consisted of 3 mm of lead disks, which were deployed either as one continuous disk or as two disks with 2 mm and 1 mm thickness, respectively. The latter two target disks, which were separated by 10 cm along the beam, allowed additional systematic studies. The present analysis uses events recorded with the so-called multiplicity trigger that selects at least two charged outgoing particles at scattering angles smaller than 50 mrad. For this purpose, a scintillator disk of 5 mm thickness and a diameter of 5 cm was placed about 62 cm downstream of the target. The hits in this scintillator had to be in coincidence with the beam trigger and an energy deposit of several GeV in the hadronic calorimeter HCAL2.

For the present data analysis, events are required to have exactly three charged outgoing particles with charge signature $(--+)$. These are assumed to be pions. A common vertex fit between these particles and the incoming

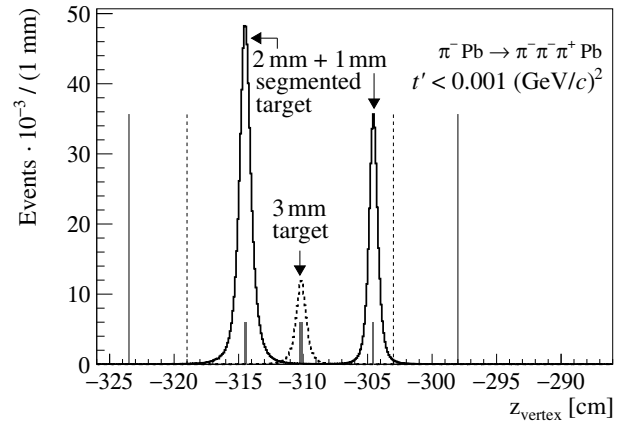


Fig. 2. Distribution of the vertex positions along the beam axis for the 3π final-state events with $t' < 0.001 (\text{GeV}/c)^2$. The distributions of the reconstructed vertices for the two target setups (solid and dashed lines) are complemented with vertical thin lines indicating the cuts applied to the respective data sets. The grey boxes represent the nominal thicknesses and positions of the target disks. The numbers of entries in the two histogram sets reflect the different measurement times with the two target setups.

beam particle must be consistent with an interaction in the lead target as indicated in fig. 2. The summed energy of the three outgoing pions $E_{3\pi}$ needs to match the mean beam energy within $\pm 4 \text{ GeV}$ to assure an exclusive $\pi^- \text{Pb} \rightarrow \pi^- \pi^- \pi^+ \text{Pb}$ reaction. About 1 million events were recorded with $t' < 0.001 (\text{GeV}/c)^2$, *i.e.* in the Primakoff t' region. Their invariant 3π mass spec-

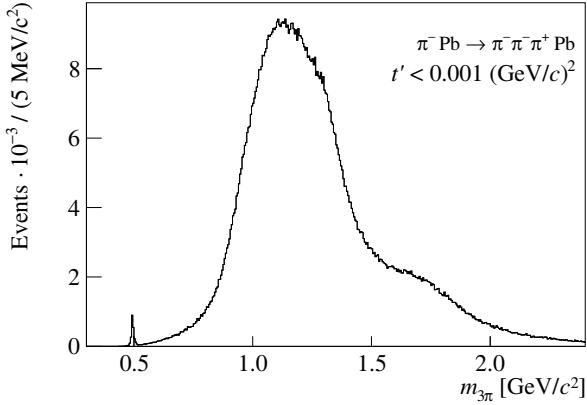


Fig. 3. Invariant mass spectrum of the 3π final-state events with $t' < 0.001 (\text{GeV}/c)^2$. The sharp peak at $m_{3\pi} \approx 0.493 \text{ GeV}/c^2$ originates from in-flight decays of beam kaons into the investigated final state.

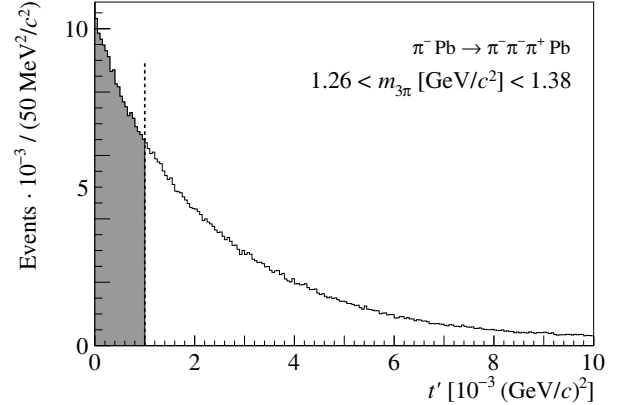
trum is shown in fig. 3, where the main contributions from diffractive production of the $a_1(1260)$ and $\pi_2(1670)$ resonances are clearly visible. The low-mass region $m_{3\pi} < 0.72 \text{ GeV}/c^2$ has been the focus of the measurement of chiral dynamics using the same data set [11]. The small peak at $m_{3\pi} \approx 0.493 \text{ GeV}/c^2$ originates from the in-flight decays of beam kaons into $\pi^- \pi^- \pi^+$.

For the extraction of the resonant components contained in this mass spectrum, a partial-wave analysis (PWA) is carried out as summarised in sect. 2.1. The specific features of a PWA at very low t' are summarised in sect. 2.2, followed by the presentation of the Primakoff production of $a_2(1320)$ and $\pi_2(1670)$ in sect. 2.3. The momentum transfer distributions for the investigated mass regions, *i.e.* $1.26 \text{ GeV}/c^2 < m_{3\pi} < 1.38 \text{ GeV}/c^2$ containing the $a_2(1320)$ and $1.50 \text{ GeV}/c^2 < m_{3\pi} < 1.80 \text{ GeV}/c^2$ containing the $\pi_2(1670)$, are presented in fig. 4. A sharp increase is observed with $t' \rightarrow 0$, where the Primakoff process contributes in addition to the dominant diffractive production. These figures demonstrate the necessity of special methods to extract the Primakoff process.

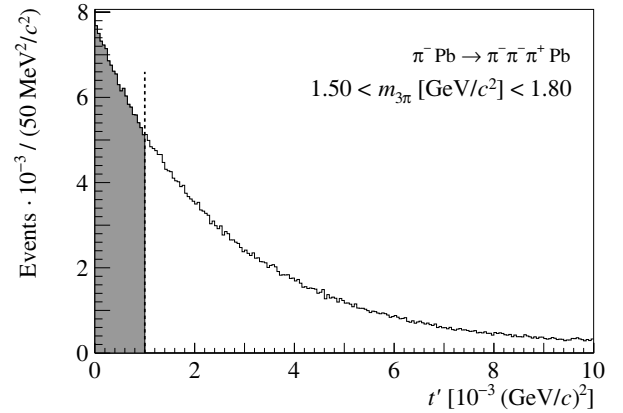
2.1 Partial-wave analysis of the $\pi^- \pi^- \pi^+$ system at very low t'

In the first step of the partial-wave analysis, the data are divided into bins of the invariant three-pion mass that in the following is denoted by m . The experimentally observed cross section $\Delta\sigma_m(\tau, t')$, in terms of acceptance-corrected intensity, is parameterised by

$$\Delta\sigma_m(\tau, t') = \frac{1}{L \epsilon_X \epsilon_{\text{resol}}} \times \sum_{\epsilon=\pm 1} \sum_{r=1}^{N_r} \left| \sum_i T_{ir}^\epsilon(m) \bar{f}_i^\epsilon(t', m) \bar{\psi}_i^\epsilon(\tau, m) \right|^2. \quad (6)$$



(a)



(b)

Fig. 4. Momentum transfer distributions in the investigated mass regions containing (a) the $a_2(1320)$ or (b) the $\pi_2(1670)$. The Primakoff region, $t' < 0.001 (\text{GeV}/c)^2$, is highlighted.

The symbol $\bar{\psi}_i^\epsilon(\tau, m)$ denotes the normalised decay amplitude of a particular partial wave i , depending only on τ within the mass bin. Here, τ is the vector of the independent phase-space variables that parameterise the final-state kinematics, *i.e.* 5-dimensional for a three-body final state. The normalisation of the decay amplitude is chosen such that the integral of the amplitude squared over the full phase space is equal to 1. Each decay amplitude is multiplied by its corresponding t' dependence $\bar{f}_i^\epsilon(t', m)$:

$$\bar{\psi}_i^\epsilon(\tau, m) = \frac{\psi_i^\epsilon(\tau, m)}{\sqrt{\int |\psi_i^\epsilon(\tau, m)|^2 d\Phi(\tau)}}$$

and

$$\bar{f}_i^\epsilon(t', m) = \frac{f_i^\epsilon(t', m)}{\sqrt{\int |f_i^\epsilon(t', m)|^2 dt'}}. \quad (7)$$

The t' dependences are either following the experimental data or are obtained from a dedicated Monte Carlo study as explained later. At this stage, also resolution effects

of the spectrometer are taken into account. The complex-valued numbers $T_{ir}^\epsilon(m)$ in eq. (6) are the transition amplitudes that represent the strengths of the individual amplitudes i and their phases. They are assumed to be constant within each mass bin so that $\Delta\sigma_m$ depends only on the phase-space parameter vector τ . The parameterisation of the cross section is optimised using T_{ir}^ϵ as fitting parameters in an extended maximum-likelihood fit, taking into account the geometrical acceptance of the spectrometer obtained from a dedicated Monte Carlo simulation as described in appendix A.1. Since the PWA is performed in bins of mass m or momentum transfer t' , respectively, resolution effects in these variables are not unfolded by the employed acceptance correction.

The decay amplitudes $\psi_i^\epsilon(\tau, m)$ of the three-pion final states are parameterised in the isobar model by subsequent two-particle decays, *i.e.* the three-pion resonance decays first into a single π^- and a di-pion resonance, referred to as the isobar in the following, which decays further into a $\pi^+\pi^-$ pair. The amplitudes are given in the Gottfried-Jackson reference system [12, 13] and denoted as $J^{PC}M^\epsilon\{\text{isobar}\}[L]\pi$, giving the quantum numbers of the three-pion resonance J^{PC} , its spin projection M onto the beam axis, its reflectivity ϵ , the isobar, and the angular momentum L between the isobar and the unpaired π^- . The amplitudes are Bose-symmetrised in the two π^- .

The reflectivity $\epsilon = \pm 1$ describes the symmetry or antisymmetry of the decay amplitude under a reflection through the production plane. In the so-called reflectivity basis the amplitudes have the quantum numbers ϵ and $M \geq 0$ [14]. They are combinations of the two amplitudes with the customary quantum numbers $+M$ and $-M$. Parity conservation demands that the two contributions $\epsilon = \pm 1$ are added incoherently. Natural parity of the exchange particle holds for the photon (with total spin and parity $J^P = 1^-$) and the pomeron (Regge trajectory with $P = (-1)^J$), and this leads to the expectation of observing only $\epsilon = +1$. The assumption of natural parity exchange leads to the appearance of $J^{PC} = 2^{++}$ resonances only with $M = 1$, while *e.g.* for $J^{PC} = 2^{-+}$ resonances both $M = 0$ and $M = 1$ are allowed.

The rank N_r introduces the number of independent sets of coherent amplitudes. Choosing $N_r > 1$ allows effectively for incoherence between contributing partial waves as expected, *e.g.*, for different helicity final states of the unobserved recoil particle. However, in the kinematic range under investigation we do not expect this to play a role as we expect coherent scattering on the whole nucleus, and thus set $N_r = 1$. Nevertheless, apparent incoherence effects occur due to resolution. These are taken into account by the partial-coherence concept that is explained in appendix A.2.

The physical parameters are extracted from the spin-density matrix

$$\rho_{ij}^\epsilon = \sum_r T_{ir}^\epsilon T_{jr}^{\epsilon*}. \quad (8)$$

In particular, its diagonal elements determine the intensities \mathcal{I}_i of the specific amplitudes i , and the relative phases φ_{ij} between two amplitudes i and j are contained in the

non-diagonal elements ($i \neq j$):

$$\mathcal{I}_i^\epsilon = \rho_{ii}^\epsilon \quad \text{and} \quad \rho_{ij}^\epsilon = |\rho_{ij}^\epsilon| e^{i\varphi_{ij}^\epsilon}. \quad (9)$$

A partial-wave analysis of data covering only the very low momentum transfer t' , as carried out here for the extraction of Primakoff contributions, has two particular features in addition to the resolution effects that are discussed later.

First, there are two production mechanisms contributing at $t' \approx 0$, diffractive and Primakoff production. They can be distinguished by the spin-projection M of the produced system. The t' dependence of the cross section for diffractively produced states with spin-projection M is given [15] by

$$d\sigma/dt' \propto t'^M e^{-b(m)t'} \quad (\text{with } M \geq 0), \quad (10)$$

where $b(m)$ is the slope that depends on the mass m of the produced system as well as on the size of the target nucleus. Thus for events at lowest momentum transfer $t' < 0.001$ (GeV/c)², only intermediate states with $M = 0$ are produced diffractively, while diffractive production with $M = 1$ is expected to be negligible. Primakoff production populates intermediate states with $M = 1$ as the helicities of quasi-real photons are $\lambda_\gamma = \pm 1$. The spin projection $M = 0$ is suppressed for quasi-real photons of very small virtuality. Following the assumptions listed above, the t' dependences $f_i^\epsilon(t', m)$ will follow a pure diffractive behaviour for $M = 0$ amplitudes and the pure Primakoff shape folded with the experimental resolution in case of $M = 1$ (see sect. 2.2).

Secondly, in addition to the (isobaric) decays of resonances there are non-resonant scattering processes populating the same final state. In the case of quasi-real photon exchange and for the low-mass region, these processes can be calculated in Chiral Perturbation Theory (ChPT) [16, 17]. This was implemented as special amplitudes to the PWA, and the tree-level calculations were probed successfully up to $m_{3\pi} \leq 0.72$ GeV/c², see ref. [11]. Higher-order ChPT calculations include loops and ρ contributions. They are expected to describe further non-resonant contributions at higher masses, and thus are used for the present analysis in addition to the chiral amplitude used in the low-mass analysis [11] (see appendices A.3, A.4, and table 4).

2.2 Features of t' spectra at values of very low t' and resolution effects

Due to the high energy of the incoming beam, the outgoing particles are strongly boosted in the forward direction, and the opening angles between the decay particles of the $\pi^-\pi^-\pi^+$ final state are small. At very low momentum transfer $t' \approx 0$, the scattering angle between the incoming pion and the produced resonance is extremely small, making the measurement sensitive to resolution effects.

The impact of the finite t' resolution was studied using a dedicated Monte Carlo (MC) simulation. Events generated with a t' dependence according to eq. (1) have been

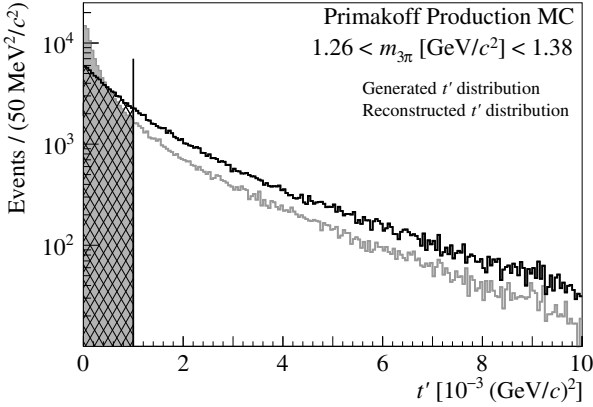


Fig. 5. Illustration of the migration of events due to the limited resolution of the spectrometer in t' . The simulated events follow the cross section given by eq. (1) with the form factor introduced in sect. 1, as given by refs. [7,8] and [9]. For details see text.

processed using the full chain of the simulation and reconstruction software. The distribution of both the generated and the reconstructed values of t' of those events that pass all analysis cuts are depicted in fig. 5 for the mass window around the mass of the $a_2(1320)$ as an example. The original shape of the cross section with a sharp peak at t_{\min} is modified significantly. For $t' < 0.001 (\text{GeV}/c)^2$, an approximately exponential behaviour $d\sigma_{\text{rec,Primakoff}}/dt' \propto \exp(-b_{\text{prim}}(m)t')$ is observed for the reconstructed Primakoff MC events. The slope parameter $b_{\text{prim}}(m)$ was found to change from $b_{\text{prim}}(0.5 \text{ GeV}/c^2) \approx 1500 (\text{GeV}/c)^{-2}$ to $b_{\text{prim}}(2.5 \text{ GeV}/c^2) \approx 700 (\text{GeV}/c)^{-2}$. This experimentally expected t' dependence is imposed on the Primakoff amplitudes in the PWA by the factor $\bar{f}_i^\epsilon(t', m)$ in eq. (6) with $f_i^\epsilon(t', m) = \exp(-\frac{1}{2}b_{\text{prim}}(m)t')$ for all amplitudes with $M = 1$. In addition, the rescaling factor ϵ_{resol} in eq. (5), which takes into account the migration of events above or below the upper t' limit, is estimated from this study. This rescaling factor complements the calculation of C_X used in eq. (5) when integrating eq. (2) over t' as shown in eq. (4). Figure 5 depicts the distribution following the cross section not containing resolution effects in grey and the experimentally expected distribution marked in black. Both histograms are based on the properties of fully reconstructed events only, as the detection and reconstruction efficiencies are expected to be taken care of by the acceptance correction of the PWA, which is denoted by ϵ_X in eq. (5). The rescaling factor ϵ_{resol} is given by the ratio of the integrals of the grey and the black-marked histograms in the indicated range $t' < 0.001 (\text{GeV}/c)^2$. It results in $\epsilon_{\text{resol}} \approx 0.74$.

The experimental t' dependence for the observed diffractive production was determined by statistical subtraction. For this method, the diffractive contribution was modelled by $d\sigma_{\text{diff}}/dt' \propto \exp(-b_{\text{diff}}(m)t')$, due to the overall predominant diffractive $M = 0$ contribution in the data. The t' distributions were modelled as described above. The full data set was divided into mass bins and fitted by

the sum of these two contributions, with $b_{\text{diff}}(m)$ as a fit parameter. The resulting trend from $b_{\text{diff}}(0.5 \text{ GeV}/c^2) \approx 420 (\text{GeV}/c)^{-2}$ to $b_{\text{diff}}(2.5 \text{ GeV}/c^2) \approx 320 (\text{GeV}/c)^{-2}$ is used for the t' dependence of the diffractive $M = 0$ amplitudes in the PWA, *i.e.* the $\bar{f}_i^\epsilon(t', m)$ in eq. (6).

An additional effect of the finite resolution at very low t' stems from the presence of two coherent production processes with very different t' dependence. The finite resolution leads to a statistical mixing of events with different t' and thus to a partial loss of the coherence between the different production amplitudes. This can be taken into account by setting the rank $N_r > 1$ in eq. (6). However, in the present analysis, amplitudes with $M = 0$ are observed to be coherent with respect to one another, as are those with $M = 1$. Thus $N_r = 1$ is actually chosen, while the reduced coherence between these two sets of amplitudes due to resolution is taken into account by the concept of partial coherence (see appendix A.2).

Furthermore, at very small t' the production plane defined by the incoming pion and the outgoing system X is known with low precision at small scattering angles. In this case, the process is almost collinear so that the production plane cannot be defined reliably and the contributions from $\epsilon = +1$ and $\epsilon = -1$ are poorly distinguishable. Thus at the limit of the extremely small t' observed for the photon peak, the full intensity of the physical $\epsilon = +1$ amplitude is reconstructed with approximately equal amounts of $\epsilon = +1$ and $\epsilon = -1$ contributions for each amplitude with $M = 1$. This introduces an artificial factor $\sqrt{2}$ in the amplitudes, which, however, is not considered separately in the following. The total intensity observed is thus contained and conserved in the incoherent sum of these two contributions as stated in eq. (6). This effect has been reproduced in a dedicated Monte Carlo simulation, with data being generated with amplitudes containing only positive reflectivity. Passing these data through the standard simulation and reconstruction chain, the same amount of negative reflectivity contributions appeared as in the experimental data.

2.3 Primakoff production of $a_2(1320)$ and $\pi_2(1670)$

The PWA results related to the Primakoff production of the $a_2(1320)$ are shown in fig. 6. The extracted intensity of the $1^{++}0^+\rho[S]\pi$ decay amplitude, which is known to contain the diffractively produced $a_1(1260)$, is shown in fig. 6(a). The intensity of the $2^{++}1^+\rho[D]\pi$ decay amplitude, where the $a_2(1320)$ is expected, is shown in fig. 6(b). The relative phase between these two amplitudes is shown in fig. 6(c). Here, the PWA was performed in $40 \text{ MeV}/c^2$ mass bins and covered $t' < 0.001 (\text{GeV}/c)^2$. The phase variation with respect to the 3π mass shows a clear rise at $m_{3\pi} \approx 1.32 \text{ GeV}/c^2$, *i.e.* at the nominal mass of the $a_2(1320)$, indicating its resonant behaviour. The change of this phase with the momentum transfer t' is extracted performing a separate PWA in bins of t' using only one mass bin that contains the major part of the $a_2(1320)$. This mass bin covers the range $1.26 \text{ GeV}/c^2 < m_{3\pi} < 1.38 \text{ GeV}/c^2$, *i.e.* it is chosen sig-

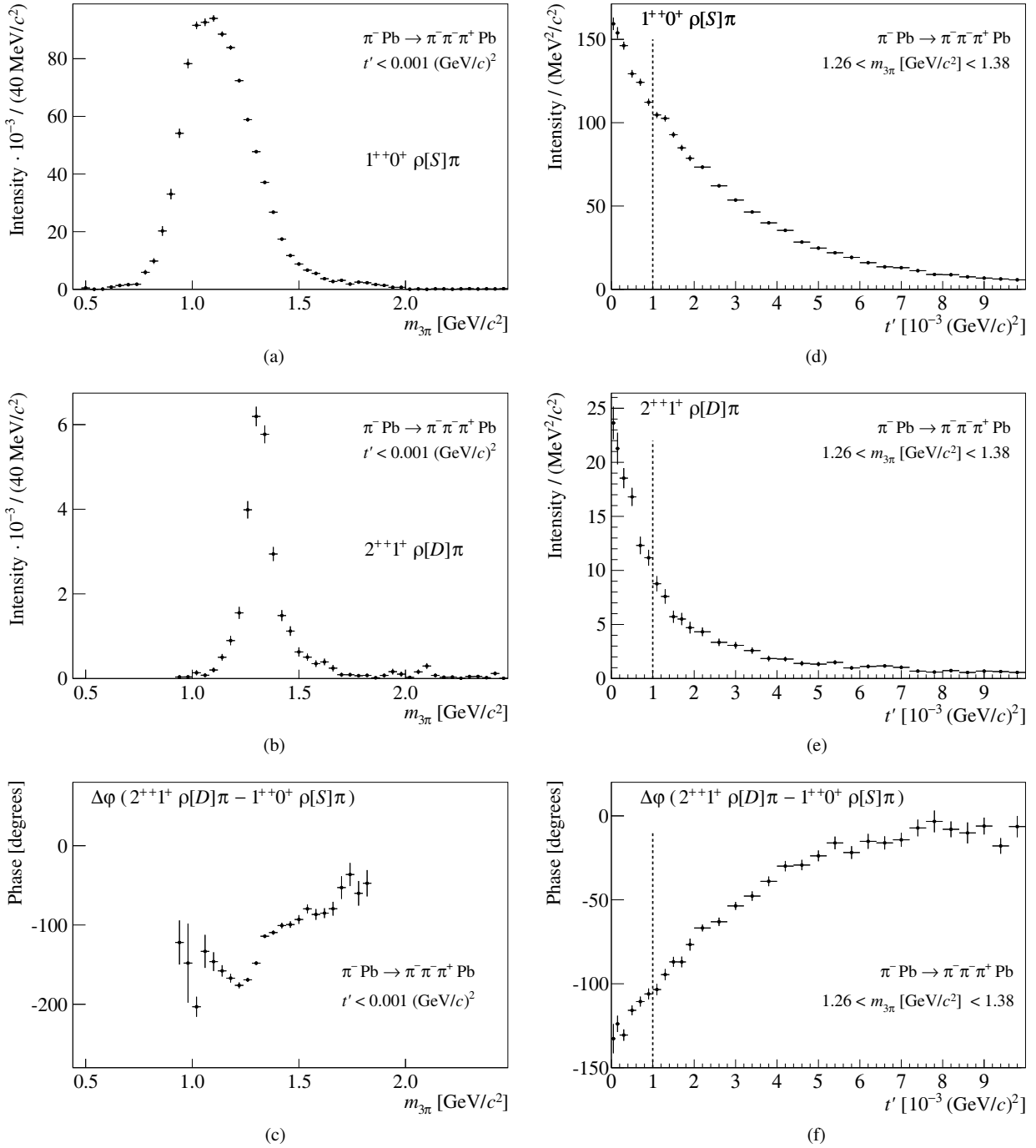


Fig. 6. Intensities of $a_1(1260)$ (top), $a_2(1320)$ (middle) and their relative phase (bottom) in bins of three-pion mass (left) and t' (right), depicting the Primakoff production of the $a_2(1320)$. For details see text.

nificantly broader than the usual $40 \text{ MeV}/c^2$. The mass dependence is introduced by the respective Breit-Wigner functions as factors in the decay amplitudes of $a_1(1260)$ and $a_2(1320)$, while t' dependences are not applied. In fig. 6(d) and (e) the resulting intensities of the same amplitudes containing the $a_1(1260)$ and $a_2(1320)$, respectively, are shown, this time in bins of t' . In fig. 6(f), the relative phase between these two decay amplitudes in bins of t' shows the transition of the production pro-

cess from Primakoff production to diffractive dissociation of the pion into the $a_2(1320)$ in the depicted range of t' . The latter is characterised by an approximately constant phase at $t' > 0.006$. In the region of interest $t' < 0.001 \text{ (GeV}/c^2)^2$, the relative phase $\Delta\phi$ of the two production amplitudes covers the range between 110° and 130° . This indicates that interference of diffractive and Primakoff production of the $a_2(1320)$ in this t' range is small.

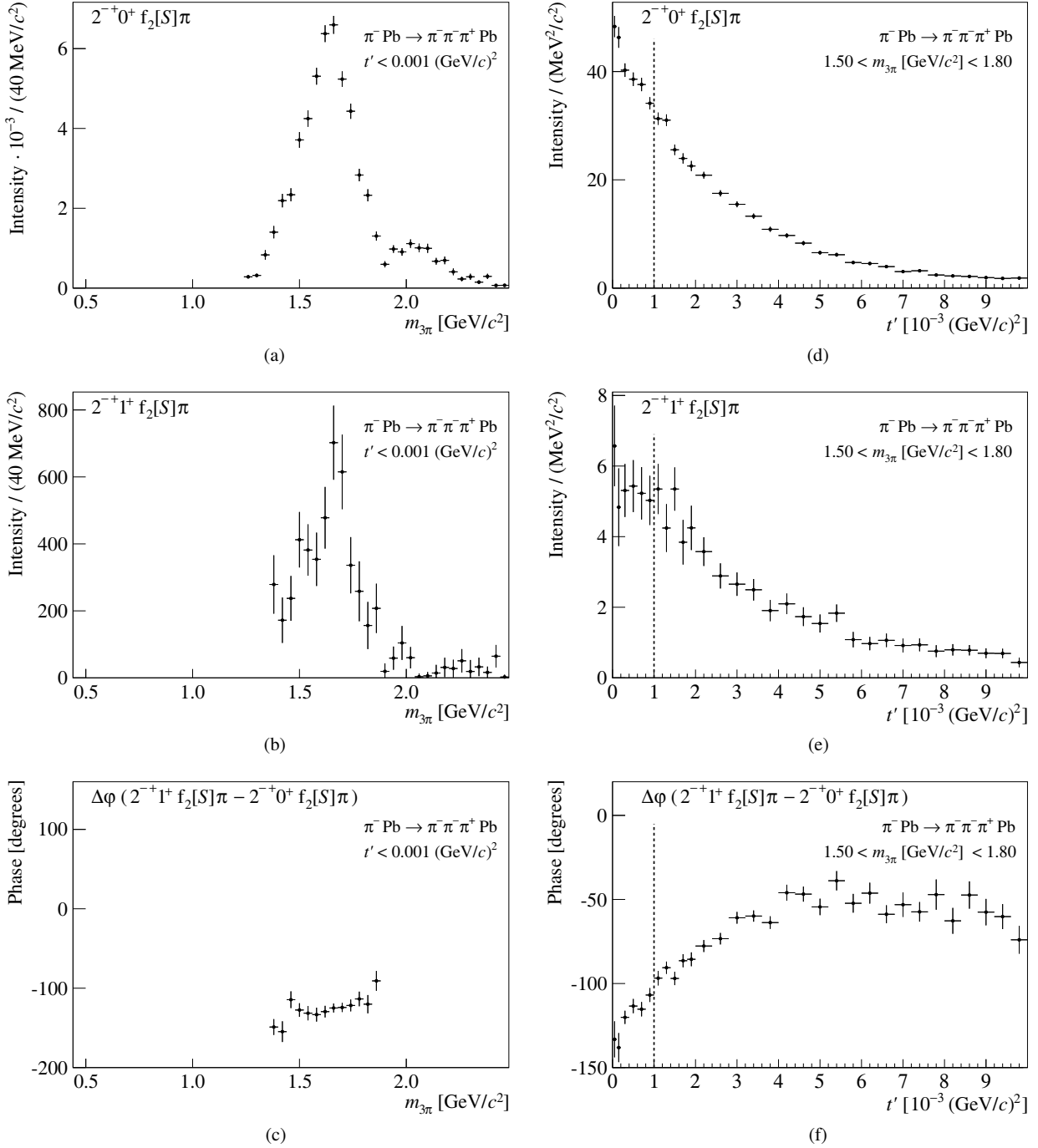


Fig. 7. Intensities of the diffractively produced $\pi_2(1670)$ with $M = 0$ (top), the $\pi_2(1670)$ with $M = 1$ (middle) and their relative phase (bottom) in bins of three-pion mass (left) and t' (right), showing the Primakoff production of the $\pi_2(1670)$ with $M = 1$. For details see text.

Figure 7(a) shows the intensity of the $2^{-+}0^{+} f_2[S]\pi$ partial wave with $M = 0$, which contains the diffractively produced $\pi_2(1670)$, and fig. 7(b) the intensity of the $2^{-+}1^{+} f_2[S]\pi$ amplitude with $M = 1$. Their relative phase as obtained from the PWA is shown in fig. 7(c) as a function of the three-pion mass. The phase shows a constant behaviour around the nominal mass of the $\pi_2(1670)$. This phase locking indicates the presence of the

same resonance $\pi_2(1670)$ in both spin projections $M = 0$ and $M = 1$, which are allowed for $J^{PC} = 2^{-+}$ amplitudes for natural parity exchange as explained before. Again, a separate PWA was performed in bins of momentum transfer t' while using a broad three-pion mass interval covering the main part of the width of the $\pi_2(1670)$, *i.e.* $1.50 \text{ GeV}/c^2 < m_{3\pi} < 1.80 \text{ GeV}/c^2$. For this PWA fit the decay amplitudes of the significant partial waves

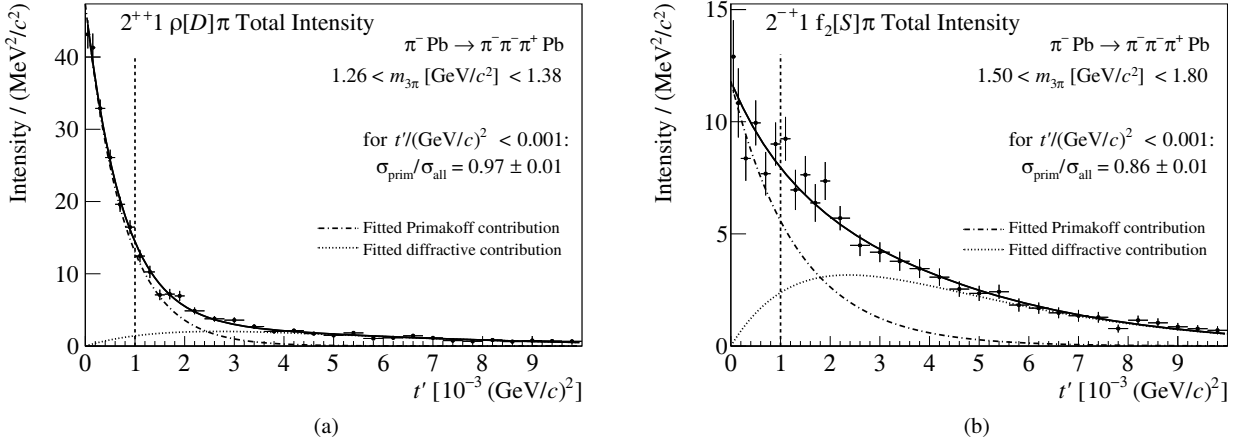


Fig. 8. Total intensities of (a) the $J^{PC}M = 2^{++}1$ and (b) the $J^{PC}M = 2^{-+}1$ states decaying into $f_2[S]\pi$ in bins of t' . Both are fitted by a sum of two exponentials to extract the fraction of Primakoff production of the $a_2(1320)$ and the $\pi_2(1670)$. The full line refers in both cases to the sum of the two contributions. For details see text.

are multiplied by mass-dependent functions containing sums of the relevant Breit-Wigner functions and additional background as given in appendix A.5. The relative phase between the $M = 0$ and $M = 1$ components of the $\pi_2(1670)$ (fig. 7(d,e,f)) demonstrates the transition from Primakoff to diffractive production of the $\pi_2(1670)$ with $M = 1$ in the depicted range of t' . Again, we observe the relative phase being approximately 90° in the region of interest $t' < 0.001 (\text{GeV}/c)^2$, which limits interference effects between diffractive and Primakoff production in this t' range. This allows the separation of the two production processes by a fit with a sum of two non-interfering contributions.

At this point we do not make any statement about resonances in $J^{PC} = 1^{++}$ or $J^{PC} = 1^{-+}$ amplitudes with $M = 1$. Such amplitudes are present in the fit (see table 4) and collect non-negligible intensities, but their interpretation in terms of resonances is not obvious. The clarification of their nature is beyond the scope of the present paper.

The total intensities of the amplitudes with $J^{PC}M = 2^{++}1$ in the $\rho[D]\pi$ and $J^{PC}M = 2^{-+}1$ in the $f_2[S]\pi$ decay channel are depicted in fig. 8. They are fitted by an incoherent sum of Primakoff and diffractive productions to obtain the relative strengths of both contributions to be evaluated in the indicated range $t' < 0.001 (\text{GeV}/c)^2$. This procedure is justified by the expected relative phase of $\approx 90^\circ$ between the photon and pomeron amplitudes, which is caused by the photon being real, while the pomeron corresponds to imaginary potential due to the absorptive nature of the strong interaction. For pomeron exchange, no phase difference between $M = 0$ and $M = 1$ amplitudes is expected. For this fit the Primakoff production is parameterised by $d\sigma_{\text{prim}}/dt' \propto \exp(-b_{\text{prim}}(m)t')$ instead of the extremely sharp form given by eq. (1), as discussed in sect. 2.2. The diffractive contribution, in turn, is parameterised by $\sigma_{\text{diff}} \propto t' \exp(-b_{\text{diff}}(m)t')$, as for $M = 1$ in eq. (10).

The resulting slopes amount to $b_{\text{prim}}(m_{a_2}) = (1292 \pm 53) (\text{GeV}/c)^{-2}$ and $b_{\text{diff}}(m_{a_2}) = (374 \pm 25) (\text{GeV}/c)^{-2}$

for the $a_2(1320)$ (fig. 8(a)). The quoted fit uncertainties take into account the error estimates from the PWA as they are indicated on the data points in fig. 8. These slope parameters are in fair agreement with the expectations from the simulation of Primakoff production, namely $b_{\text{prim,MC}} \approx 980 (\text{GeV}/c)^{-2}$ and $b_{\text{diff,MC}} \approx 370 (\text{GeV}/c)^{-2}$. These expected values are obtained following the procedure explained in sect. 2.2.

For the $2^{-+}1 f_2[S]\pi$ total intensity in the mass region of the $\pi_2(1670)$ (fig. 8(b)), the separation of the two contributions is difficult as the respective parameters are highly correlated. Therefore, in our analysis we imposed the condition that the fractions of Primakoff and diffractive contributions are equal at that value of t' , where the relative phase between the $M = 0$ and $M = 1$ amplitudes (fig. 7(f)) is 45° below the phase at $t' \approx 0.01 (\text{GeV}/c)^2$. This is approximately achieved limiting the parameter range to $b_{\text{prim}} \geq 750 (\text{GeV}/c)^{-2}$. It results in $b_{\text{diff}} = (421 \pm 20) (\text{GeV}/c)^{-2}$ and $b_{\text{prim}} = 750 (\text{GeV}/c)^{-2}$ at its lower limit, in rather good agreement with the expected values of $b_{\text{diff,MC}} \approx 350 (\text{GeV}/c)^{-2}$ and $b_{\text{prim,MC}} \approx 760 (\text{GeV}/c)^{-2}$ from the procedure described in sect. 2.2.

The ratio $\sigma_{\text{prim}}/\sigma_{\text{all}}$ is obtained by integrating the contributions in the range $t' < 0.001 (\text{GeV}/c)^2$, yielding 0.97 ± 0.01 for the $a_2(1320)$ and 0.86 ± 0.07 for the $\pi_2(1670)$. The uncertainties quoted are obtained from varying the upper and lower limits of b_{prim} and b_{diff} . For the $a_2(1320)$, fits are performed with limiting $b_{\text{prim}} \leq 980 (\text{GeV}/c)^{-2}$ and requiring $b_{\text{diff}} \geq 320 (\text{GeV}/c)^{-2}$. For the $\pi_2(1670)$, fits with b_{prim} down to $500 (\text{GeV}/c)^{-2}$ are taken into account. This is done to account for the neglect of interference between the Primakoff and the diffractive contributions.

3 Extraction of the radiative widths

For the extraction of the radiative width of a resonance, we integrate eq. (2) over the range $0 (\text{GeV}/c)^2 < t' < 0.001 (\text{GeV}/c)^2$ and over the relevant mass ranges containing the $a_2(1320)$ and $\pi_2(1670)$.

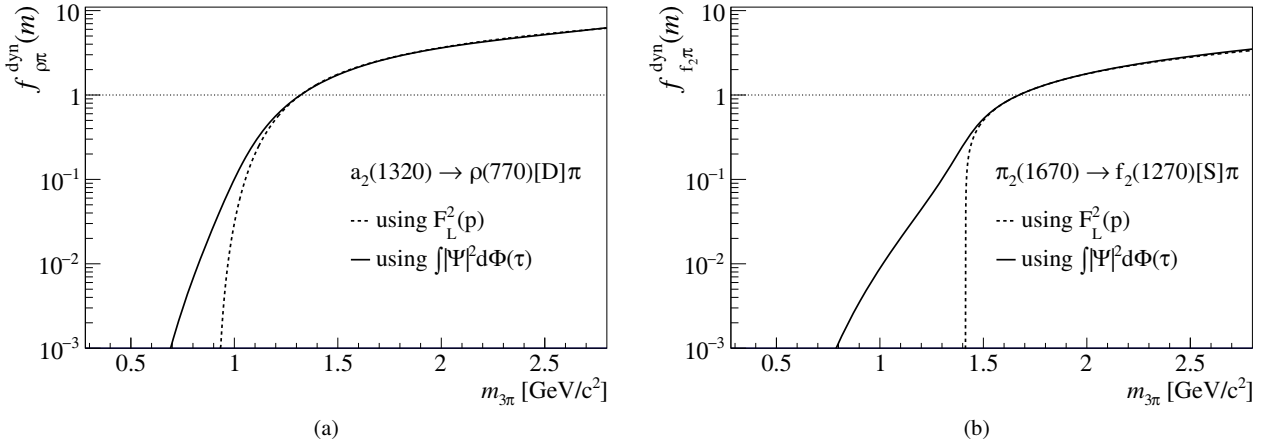


Fig. 9. Comparison of the dynamical factors for (a) the $a_2(1320) \rightarrow \rho(770)[D]\pi$ and (b) the $\pi_2(1670) \rightarrow f_2(1270)[S]\pi$ decays using angular momentum barrier factors or $\int |\psi|^2 d\Phi(\tau)$ (for details see text). The lines extent in the latter case, with non-zero values for f^{dyn} , down to the three-pion threshold $m_{3\pi} = 3m_\pi \approx 0.42 \text{ GeV}/c^2$, while in the case of F_L the range is limited to $m_{3\pi} > m_\pi + m_{\{\text{isobar}\}}$.

3.1 Parameterisation of mass-dependent widths

An important ingredient for the determination of the radiative widths is the accurate mathematical description of the mass spectra observed. Apart from the damping of higher masses introduced by t_{min} appearing in eq. (2), this concerns in particular the total and partial mass-dependent decay widths. They both enter into fits of the PWA intensities containing Breit-Wigner parameterisations, which are used for the extraction of N_X/ϵ_X and for the calculation of the normalisation constant C_X that is needed for the evaluation of eq. (5). The exact line shape has to describe properly the tails towards lower and higher masses which are very asymmetric, as we assume that those are not mocked up by background but belong to the resonances under investigation.

If a resonance decays only via two-body decays into particles, the width of which can be neglected, and if the decay channels do not interfere, the mass-dependent total width of the resonance can be written as

$$\Gamma_{\text{total}}(m) = \sum_n \Gamma_n(m) = \sum_n \text{BR}_n \underbrace{\frac{m_0 p_n F_L^2(p_n)}{m p_{0n} F_L^2(p_{0n})}}_{f_n^{\text{dyn}}(m)} \Gamma_0$$

with $\Gamma_0 \equiv \Gamma_{\text{total}}(m_0)$. (11)

This expression contains a sum over the partial widths Γ_n of all possible decay channels n of this resonance (with their corresponding normalised branching fractions BR_n). The two-body breakup momentum p_n is the momentum of the daughter particles of a particular decay n of a parent state with mass m in its centre-of-mass frame, and L is the orbital angular momentum between the two daughter particles. The symbol F_L specifies the angular momentum barrier factors as given by ref. [18]. The additional index “0” denotes the values of width and breakup momentum at the nominal mass m_0 of the resonance. In cases where the branching fractions are unknown, a Breit-Wigner func-

tion with constant width Γ_0 is usually chosen as an approximation.

A more accurate parameterisation of the mass dependence of $\Gamma_n(m)$ is preferable especially in the case of multi-particle decays with short-lived decay products, so that the widths of the daughter particles can be taken into account properly. Hence, in order to include properly also sub-threshold contributions, the term $p_n F_L^2(p_n)$ is replaced by the integral over the respective decay amplitude $\int |\psi_n|^2 d\Phi(\tau)$ [19]. The effect is depicted in fig. 9. The description using angular momentum barrier factors (from eq. (11), dashed lines) starts from the nominal {isobar} π thresholds only, which are $\approx 0.9 \text{ GeV}/c^2$ for the $\rho\pi$ decay and $\approx 1.5 \text{ GeV}/c^2$ for the $f_2\pi$ decay. The description based on $\int |\psi_n|^2 d\Phi(\tau)$ for the considered decay channels $n = \rho\pi$ and $n = f_2\pi$ starts from the summed mass of the final state particles (*i.e.* $\approx 0.42 \text{ GeV}/c^2$ for three pions), so that it describes the low-mass tail which is considerable, particularly for the $\pi_2(1670)$. In the figure and in the following, the index “ n ” is dropped for p_n and p_{0n} , and those are understood to be the appropriate breakup momenta.

In many cases, the shape of a specific resonance does not support the use of the term m_0/m in eq. (11), which introduces additional damping at higher masses. Reference [20] even suggests that the term $(m_0/m)^\alpha$ may be used with arbitrary α adjusted to the data. In this analysis, where also the damping behaviour of m resulting from the integrated t' dependences from eq. (2) is taken into account, a better fit to the mass spectrum is obtained when omitting the term m_0/m in the parameterisation of the mass-dependent widths.

The mass-dependent partial width of the $X \rightarrow \pi\gamma$ decay, $\Gamma_{\pi\gamma}(m)$, reads

$$\Gamma_{\pi\gamma}(m) = \frac{p}{p_0} \underbrace{\frac{F_L^2(p)}{F_L^2(p_0)}}_{f_{\pi\gamma}^{\text{dyn}}(m)} \Gamma_0(X \rightarrow \pi\gamma), \quad (12)$$

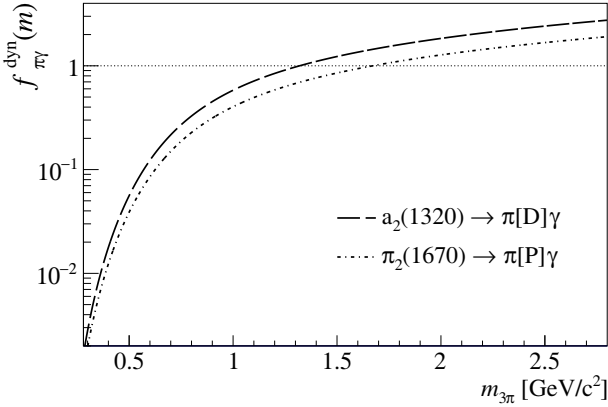


Fig. 10. Shapes of the dynamical factors $f_{\pi\gamma}^{\text{dyn}}(m)$ for the $\pi\gamma$ decays of the $a_2(1320)$ and the $\pi_2(1670)$.

where we use $L = 2$ (D -wave) and $L = 1$ (P -wave) for the $\pi\gamma$ decays of the $a_2(1320)$ and $\pi_2(1670)$ resonance, respectively. The use of the F_L -dependent factor, which is depicted in fig. 10, may be disputable. However, it has an effect of only about 1% and 3% on the final result for the $a_2(1320)$ and the $\pi_2(1670)$, respectively, compared to using $f_{\pi\gamma}^{\text{dyn}}(m) = (p/p_0)^3$ as suggested in ref. [1].

For the mass-dependent partial decay widths $\Gamma_{\text{final}}(m)$ the widths of the isobars have to be taken into account, *i.e.* they are parametrised as

$$\Gamma_{\text{final}}(m) = \frac{\int |\psi_{\text{final}}(m, \tau)|^2 d\Phi(\tau)}{\underbrace{\int |\psi_{\text{final}}(m_0, \tau)|^2 d\Phi(\tau)}_{f_{\pi\{\text{isobar}\}}^{\text{dyn}}(m)}} \times \Gamma_0(X \rightarrow \pi\{\text{isobar}\}). \quad (13)$$

The $a_2(1320)$ is observed in the total intensity of the $J^{PC}M = 2^{++}1$ waves decaying into $\rho[D]\pi$, *i.e.* $\{\text{isobar}\} = \rho(770)$ and $L = 2$, so that $\psi_{\text{final}} = \psi_{2^{++}1+\rho(770)[D]\pi}$ is used.

The total width $\Gamma_{\text{total}}(m)$ of the $a_2(1320)$ is derived from eq. (11) using the constant $\Gamma_0 = \Gamma_0(m_0(a_2))$. The total width is taken as the sum of the partial widths of the two main decay channels $\rho\pi$ and $\eta\pi$. As the other decay channels are neglected as described below, we calculate “renormalised” branching fractions BR_n from their known branching fractions BR_n^{PDG} from ref. [6]. Those are given in table 1 together with the used parameterisations of the phase space. The $\omega\pi\pi$ decay channel ($\text{BR}_{\omega\pi\pi}^{\text{PDG}} = 0.105$) and the $K\bar{K}$ decay channel ($\text{BR}_{K\bar{K}}^{\text{PDG}} = 0.049$) are not taken into account, as the treatment of the $\omega\pi\pi$ decay in the framework of two-particle decays is delicate due to unknown branching fractions into $b_1(1235)\pi$ and $\omega\rho$, which both are sub-threshold at the nominal mass of the $a_2(1320)$. The $K\bar{K}$ channel has an even smaller branching fraction than the $\omega\pi\pi$ decay channel and its radiative decay width is not included in Γ_{total} here as well due to its smallness, $\text{BR}_{\pi\gamma} < 0.01$.

The $\pi_2(1670)$ is observed in the total intensity of the $J^{PC}M = 2^{-+}1$ amplitudes decaying into $f_2[S]\pi$,

Table 1. Branching fractions BR_n^{PDG} and BR_n and parameterisations of phase space $f_n^{\text{dyn}}(m)$ for the two main decay channels $\rho\pi$ and $\eta\pi$, as used for the description of the mass-dependent total width of the $a_2(1320)$.

n	BR_n^{PDG}	BR_n	$f_n^{\text{dyn}}(m)$
$\rho[D]\pi$	0.701	0.82	$\frac{\int \psi(m) ^2 d\Phi(\tau)}{\int \psi(m_0) ^2 d\Phi(\tau)}$
$\eta[D]\pi$	0.145	0.18	$\frac{p}{p_0} \frac{F_2^2(p)}{F_2^2(p_0)}$

i.e. $\{\text{isobar}\} = f_2(1270)$ and $L = 0$, so that $\psi_{\text{final}} = \psi_{2^{-+}0+f_2(1270)[S]\pi}$ is used.

The parameterisation of the mass-dependent width of the $\pi_2(1670)$ is more complicated. The $\pi_2(1670)$ decays mainly into 3π ($\text{BR}_{3\pi}^{\text{PDG}} = 0.96$), which includes decays into $f_2\pi$ ($\text{BR}_{f_2\pi}^{\text{PDG}} = 0.56$), $\rho\pi$ ($\text{BR}_{\rho\pi}^{\text{PDG}} = 0.31$), $\sigma\pi$ ($\text{BR}_{\sigma\pi}^{\text{PDG}} = 0.11$) and $(\pi\pi)_{S\pi}$ ($\text{BR}_{(\pi\pi)_{S\pi}}^{\text{PDG}} = 0.09$) [6]. All these decays are also observed in the COMPASS experiment. However, the incoherent sum in eq. (11) is questionable for the different 3π final states, as they interfere significantly. In addition, the branching fractions BR^{PDG} are quoted for “ 3π ”, but do not distinguish between the charged and the neutral channel, where they are expected to differ due to the different isospins of ρ and f_2 . For this analysis, we only take into account the decay $\pi_2(1670) \rightarrow f_2(1270)[S]\pi$ with its branching fraction $\text{BR}_{f_2\pi}^{\text{PDG}} = 0.56$ taken from ref. [6]. For the mass-dependent width we use $\Gamma_{\text{total}}(m) = f_{\text{final}}^{\text{dyn}}(m)\Gamma_0(m_0)$ since the exact shape of the Breit-Wigner function does not matter for the signal strength of the $\pi_2(1670)$ at the current level of accuracy.

3.2 Acceptance-corrected PWA intensities

In the first step the acceptance-corrected intensities $N_{X,\text{prim}}/\epsilon_X$ used in eq. (5) are determined. The intensities in mass bins obtained from the PWA (fig. 11) are fitted by the mass-dependent Breit-Wigner terms from eq. (2), while integrating over $0(\text{GeV}/c)^2 < t' < 0.001(\text{GeV}/c)^2$. The mass-dependent widths $\Gamma_{\pi\gamma}(m)$, $\Gamma_{\text{final}}(m)$ and $\Gamma_{\text{total}}(m)$ are evaluated using the terms $f_{\pi\gamma}^{\text{dyn}}(m)$, $f_{\pi\{\text{isobar}\}}^{\text{dyn}}(m)$, and $\sum_n \text{BR}_n f_n^{\text{dyn}}(m)$ as explained in sect. 3.1, m_0 and Γ_0 are introduced as fit parameters, and $\Gamma_0(X \rightarrow \pi\gamma)$ is contained in the fit parameter for the overall normalisation of the Breit-Wigner. In the fitting procedure the bin width of $40 \text{ MeV}/c^2$ and the mass resolution are taken into account. The mass resolution amounts to $\approx 16 \text{ MeV}/c^2$ for the $a_2(1320)$ and $\approx 18 \text{ MeV}/c^2$ for the $\pi_2(1670)$. More precisely, the mass resolutions of both resonances are parameterised by a sum of three Gaussian distributions, the parameters of which were obtained from the MC simulation described in sect. 2.2. The fit to the intensities shown in fig. 11 yields the following parameters. For the $a_2(1320)$ we obtain the mass $m_0 = (1319 \pm 1) \text{ MeV}/c^2$ and the width $\Gamma_0 = (105 \pm 4) \text{ MeV}/c^2$ with a fit quality of $\chi^2/\text{NDF} = 59.9/24$,

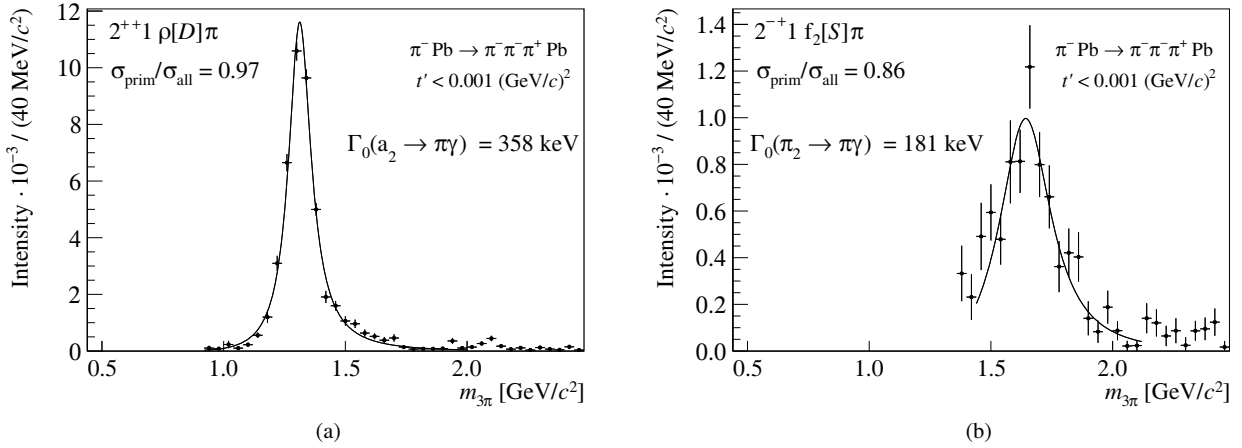


Fig. 11. Total intensities in mass bins: $J^{PC}M = 2^{++}$ from $\rho[D]\pi$ decay and $J^{PC}M = 2^{-+}$ from $f_2[S]\pi$ decay. The error bars show the statistical uncertainties of the PWA. The Breit-Wigner fits used for the determination of the intensities of (a) the $a_2(1320)$ and (b) the $\pi_2(1670)$ are shown as well.

and for the $\pi_2(1670)$ the mass $m_0 = (1684 \pm 11) \text{ MeV}/c^2$ and the width $\Gamma_0 = (277 \pm 38) \text{ MeV}/c^2$ with a fit quality of $\chi^2/\text{NDF} = 20.0/14$.

From these fits, the following acceptance-corrected integrated intensities N_X/ϵ_X are obtained that are used for the evaluation of eq. (5). The intensity for the $a_2(1320)$ ($2^{++}1\rho[D]\pi$) is integrated over the range $0.92 \text{ GeV}/c^2 < m_{3\pi} < 2.00 \text{ GeV}/c^2$ using the fit function shown in fig. 11, which results in $N_{a_2}/\epsilon_{a_2} = 44601 \pm 798$. The uncertainty represents the statistical uncertainty of the PWA fits in mass bins, which is propagated to the parameters of the Breit-Wigner fit. After the correction for $\sigma_{\text{prim}}/\sigma_{\text{all}} = 0.97$ we obtain the number of Primakoff-produced events $N_{a_2,\text{prim}}/\epsilon_{a_2} = 43262 \pm 774$. The number of $\pi_2(1670)$ events is taken from the $2^{-+}1f_2[S]\pi$ intensity integrated over the range $1.44 \text{ GeV}/c^2 < m_{3\pi} < 2.12 \text{ GeV}/c^2$, which results in $N_{\pi_2}/\epsilon_{\pi_2} = 6977 \pm 435$. Applying $\sigma_{\text{prim}}/\sigma_{\text{all}} = 0.86$, the number of Primakoff-produced $\pi_2(1670)$ is $N_{\pi_2,\text{prim}}/\epsilon_{\pi_2} = 6000 \pm 374$ in this decay channel.

3.3 Normalisation constants

In order to calculate the normalisation constant C_X , which is needed for the evaluation of eq. (5), we apply eqs. (2) and (4) using $\Gamma(\pi\gamma) = f_{\pi\gamma}^{\text{dyn}}(m) \Gamma_0(X \rightarrow \pi\gamma)$, with $f_{\pi\gamma}^{\text{dyn}}(m)$ from eq. (12), $\Gamma_{\text{final}}(m)$ as given in eq. (3) with $f_{\text{final}}^{\text{dyn}}(m) = f_{\pi\{\text{isobar}\}}^{\text{dyn}}(m)$ from eq. (13) and (CG BR) divided out here, and $\Gamma_{\text{total}}(m)$ as given in sect. 3.1. The constant is obtained integrating over the same mass range $m \in [m_1, m_2]$ as used for the extraction of N_X/ϵ_X , and over $0 \text{ (GeV}/c)^2 < t' < 0.001 \text{ (GeV}/c)^2$ which reflects the t' cut that is applied to the data:

$$C_X = \int_{m_1}^{m_2} \int_0^{t'_{\text{max}}} 16\alpha Z^2 (2J+1) \left(\frac{m}{m^2 - m_\pi^2} \right)^3 \frac{t'}{(t' + t_{\text{min}})^2} \times \frac{m_0^2 f_{\pi\gamma}^{\text{dyn}}(m) f_{\text{final}}^{\text{dyn}}(m) \Gamma_0(m_0)}{(m^2 - m_0^2)^2 + m_0^2 \Gamma_{\text{total}}^2(m)} F_{\text{eff}}^2(t') dt' dm. \quad (14)$$

For the numbers given in the following, the form factor $F_{\text{eff}}^2(t')$ and the Weizsäcker-Williams term are replaced by $|F_C^u(t', t_{\text{min}})|^2$ from refs. [7, 8] as discussed before. For C_{a_2} we use $m_0 = 1320 \text{ MeV}/c^2$, $\Gamma_0(m_0) = 107 \text{ MeV}/c^2$, and obtain $C_{a_2} = 2236.23 \text{ mb}/\text{GeV}$. The constant C_{π_2} is calculated using $m_0 = 1672 \text{ MeV}/c^2$, $\Gamma_0(m_0) = 260 \text{ MeV}/c^2$, and $\Gamma_{\text{total}}(m)$ is evaluated using the decay into $f_2\pi$ only, which results in $C_{\pi_2} = 579.83 \text{ mb}/\text{GeV}$.

3.4 Luminosity determination using the beam kaon flux

The determination of the absolute production cross section of the $a_2(1320)$ and the $\pi_2(1670)$ requires the knowledge of the luminosity, *i.e.* the (well-known) thickness of the lead target and the incoming beam flux. This flux is not monitored precisely, and the absolute trigger and detector efficiencies are only partly known, so that the absolute beam flux is not determined reliably for the present data. Instead, the effective beam flux, which takes into account spill structure and dead time, is determined with good precision by using $K^- \rightarrow \pi^- \pi^- \pi^+$ decays observed in the target region. These decays originate from the kaon component in the negative hadron beam and are contained in the data set preselected for the 3π production analysis, *i.e.* in the same final state (see fig. 3). As the systematics concerning trigger and detector efficiencies are the same as for the 3π production from incoming pions, they cancel in the ratio of the two data sets.

For better statistical precision, the cut on the decay vertex position is relaxed with respect to the usual cut for interactions in the target. Figure 12(a) presents the resulting invariant 3π mass spectrum that shows a clean kaon signal at $m_{3\pi} \approx 0.493 \text{ GeV}/c^2$. The number of kaons observed is obtained after subtraction of the small background that is estimated by a linear fit to the mass spectrum near the peak and extrapolated beneath the kaon signal.

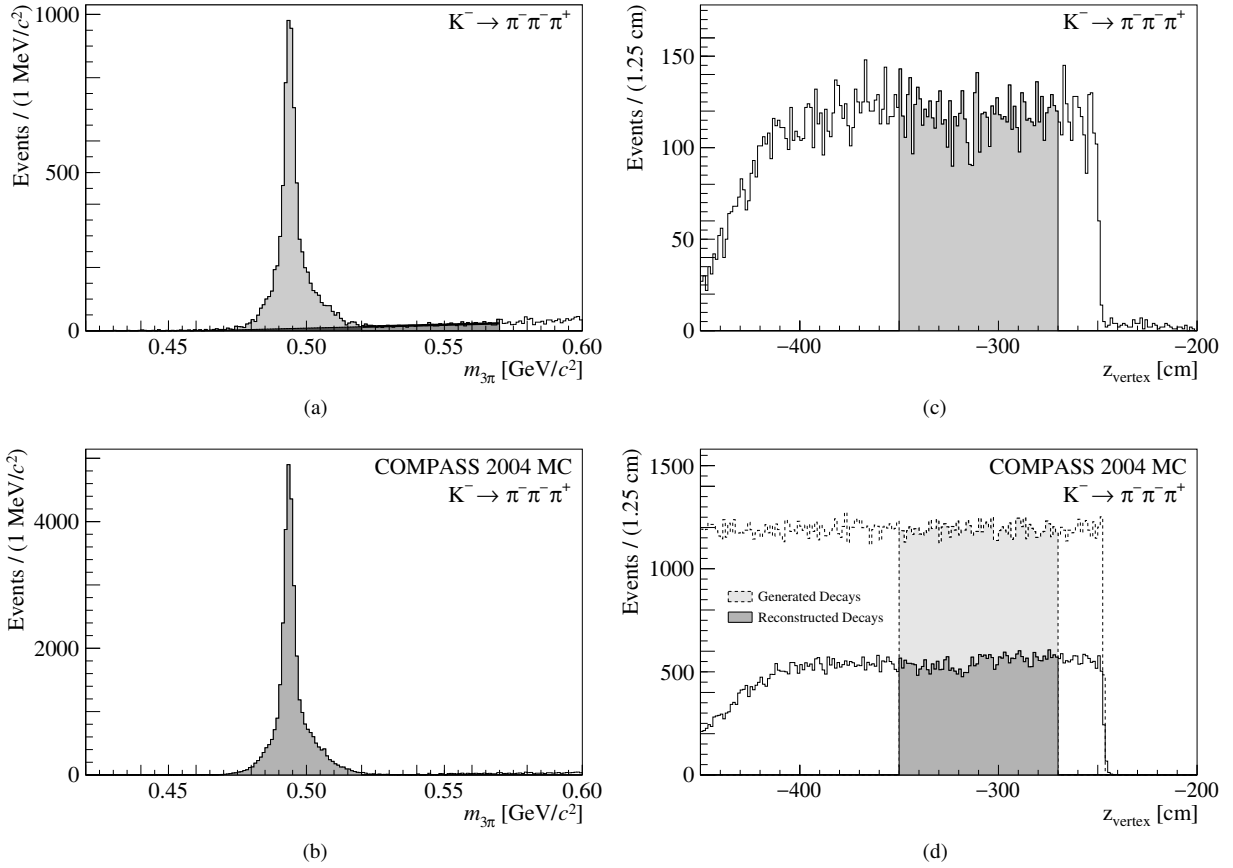


Fig. 12. Luminosity determination from the in-flight decays of beam kaons. Reconstructed invariant mass spectrum (a) and decay vertex positions (c) for the real data, and for simulated kaon decays in the target region (b,d).

The corresponding decay vertex distribution in fig. 12(c) demonstrates that these vertices are reconstructed in free space along the beam direction. At the downstream (right) edge the distribution vanishes at the position of the charged-particle multiplicity counter acting as the trigger counter. At the upstream (left) edge the positions of the beam telescope detectors measuring an incoming beam track limit the fiducial decay volume. The contribution of the small background stemming from pion interactions in the lead target is obtained from the vertex distribution in the neighbouring mass region $0.52 \text{ GeV}/c^2 < m_{3\pi} < 0.57 \text{ GeV}/c^2$ as indicated in fig. 12(a), scaled according to the expected intensity below the peak of the mass spectrum, and subtracted. The resulting distribution is quite flat, as expected, but shows a small drop in the region just upstream of the lead target. This can be explained by multiple scattering of the three pion tracks in lead, which leads to a local broadening of the decay vertex distribution. The choice of the range of positions of reconstructed decay vertices in $[-350, 270]$ cm (shaded area in fig. 12(c)) assures uniform reconstruction efficiency.

These mass and decay vertex distributions were confirmed by a dedicated full MC simulation of kaon decays in the respective region of the COMPASS spectrometer. Figure 12(b) depicts the corresponding invariant mass distribution of the reconstructed kaon decays. The contribution

Table 2. Summary of estimated statistical and systematic uncertainties for the measurement of the radiative widths of $a_2(1320)$ and $\pi_2(1670)$.

	$a_2(1320)$	$\pi_2(1670)$
Statistical	1.8%	6.2%
Systematic		
Diffractive background	1.2%	7.4%
Kaon normalisation	6.0 %	6.0 %
PWA models	5.0%	7.7%
Parameterisation mass-dep. fit	3.2%	3.1%
Radiative corrections	8.0 %	8.0%
Quadratic sum	11.7%	15.0%

from pion interactions in the target, which is present in the experimental data as smoothly rising background, is absent here. The shape of the reconstructed kaon mass spectrum is precisely reproduced, including the broad part at the base which is traced back to kaons decaying upstream of the lead target. Figure 12(d) presents the spatial distribution of simulated and reconstructed kaon decay vertices, confirming the correct choice of the fiducial decay volume.

Table 3. The values for the radiative widths of the $a_2(1320)$ and the $\pi_2(1670)$ from this analysis, compared to previous measurements and theoretical predictions.

	$a_2(1320)$	$\pi_2(1670)$
This measurement	$(358 \pm 6 \pm 42)$ keV	$(181 \pm 11 \pm 27)$ keV $\cdot (0.56/\text{BR}_{f_2\pi})$
SELEX [21]	$(284 \pm 25 \pm 25)$ keV	
S. Cihangir <i>et al.</i> [24]	(295 ± 60) keV	
E.N. May <i>et al.</i> [25]	(0.46 ± 0.11) MeV	
VMD model [1]	(375 ± 50) keV	
Relativ. Quark model [2]	324 keV	
Cov. Osc. Quark model [3]	235 keV	
Cov. Osc. Quark model [4]	237 keV	2 values: 335 keV and 521 keV

The acceptance for kaon decay events is $\epsilon_K \approx 0.459$, calculated from the ratio of number of reconstructed kaon decays (with all cuts applied) to simulated decays in the same spectrometer region as used for the kaon flux analysis of the experimental data. Using the thickness of the lead target of 3 mm, we determine the integrated effective luminosity

$$\epsilon_K L = \epsilon_K \int \mathcal{L} dt = 9.55 \times 10^4 \text{ mb}^{-1}. \quad (15)$$

The relative uncertainty on this number is estimated to be 6%, with contributions from the uncertainty of the kaon fraction in the negative hadron beam of about 5%, an uncertainty on the branching fraction of $K^- \rightarrow \pi^+\pi^-\pi^-$ of less than 1%, and the uncertainty on the number of kaon decays in the analysed data set of less than 1%. The statistical uncertainty of the luminosity determination is added in quadrature to the linear sum of the two other uncertainties.

3.5 Results

The radiative widths for both resonances are calculated using eq. (5) with the corresponding cross sections given by eq. (4). For the $a_2(1320)$, the radiative width is calculated using the parameter $\epsilon_{\text{resol}} = 0.742$ determined by the Monte Carlo simulation shown in sect. 2.2, $\text{BR}_{\rho\pi}^{\text{PDG}} = 0.701$, and the squared Clebsch-Gordan coefficient $\text{CG} = \frac{1}{2}$. The obtained value for the radiative width is $\Gamma_0(a_2 \rightarrow \pi\gamma) = 358$ keV. The radiative width of the $\pi_2(1670)$ is determined using $\text{BR}_{f_2\pi}^{\text{PDG}} = 0.56$, $\text{CG} = \frac{2}{3}$, $\epsilon_{\text{resol}} = 0.736$, which results in $\Gamma(\pi_2 \rightarrow \pi\gamma) = 181$ keV depending on the true $\text{BR}_{f_2\pi}$, *i.e.* to be multiplied by $0.56/\text{BR}_{f_2\pi}$.

The relative statistical and systematic uncertainties are summarised in table 2. The statistical uncertainties are obtained from the uncertainty of the Breit-Wigner fits to the related total intensities from fig. 11. The systematic uncertainties have five contributions that are added in quadrature. The uncertainties on the fraction of diffractive background, determined by $\sigma_{\text{prim}}/\sigma_{\text{all}}$, and the uncertainty from the kaon normalisation were discussed above.

The systematic uncertainties related to the variation of the model used for the PWA fits were derived comparing the total intensities obtained from models using either different thresholds for the $1^{++}1$ amplitudes or an additional $2^{++}0^- \rho[D]\pi$ amplitude with respect to the nominal fit model. The parameterisation of the mass-dependent

widths covers again several aspects. The systematic uncertainty related to the fits determining the resonance parameters via Breit-Wigner functions covers different parameterisations of the mass dependence of the widths, as well as the inclusion or omission of the factor m_0/m and/or the t_{min} dependent term. The differences between the parameterisation of the phase space by the traditional angular momentum barrier factors and the phase space respecting the non-zero width of the isobars were evaluated. In addition, for the $a_2(1320)$ we take into account also the difference between our approach and a simplistic description of the $a_2(1320)$ shape given by the decay into $\rho\pi$ only (*i.e.* neglecting the $\eta\pi$ decay), as implemented, *e.g.*, in ref. [21]. The fifth contribution to the systematic uncertainties originates from radiative corrections as discussed below. The employed PWA tools did not include possible relativistic effects on the amplitude parameterisation as described in ref. [22].

There exists no full QED correction of the pion and resonance interaction with the lead nucleus as $Z\alpha$ is “not small”. From the size of the correction of about 20% and the omission of any further radiative corrections, as in ref. [11], we conservatively estimate an 8% contribution to the systematic uncertainty [23]. As the only way to reduce this uncertainty, we see a measurement on a medium-heavy nucleus, where the Primakoff contribution is still sizeable but the discussed Coulomb correction has a minor impact.

Our final results for the radiative widths of the $a_2(1320)$ and the $\pi_2(1670)$ are listed in table 3. Here and in the following, the first uncertainty denotes the statistical and the second the systematic one. The value for the $a_2(1320)$ is $\Gamma_0(a_2(1320) \rightarrow \pi\gamma) = (358 \pm 6 \pm 42)$ keV, where $|F_C^u(t', t_{\text{min}})|^2$ from refs. [7, 8] is used. If $F_{\text{eff}}^2(t')$ in eq. (2) is approximated as $F_{\text{eff}}^2(t') = j_1^2(t')$ for the lead target, *i.e.* the Coulomb correction is not applied, we obtain $\Gamma_0(a_2(1320) \rightarrow \pi\gamma) = (312 \pm 6)$ keV. Most earlier measurements reported lower values compatible with this value as given in table 3. The authors of ref. [21] report to have taken into account the Coulomb corrections and they estimated that it had “minor impact” on their result (see table 3). Our calculation, however, shows that the effect is 24% for our experiment and 15% for the conditions of the SELEX experiment. The result for the $\pi_2(1670)$ is $\Gamma_0(\pi_2(1670) \rightarrow \pi\gamma) = (181 \pm 11 \pm 27)$ keV $\cdot (0.56/\text{BR}_{f_2\pi})$.

In the case that $F_{\text{eff}}^2(t') = j_1^2(t')$ is used, we calculate $\Gamma_0(\pi_2(1670) \rightarrow \pi\gamma) = (151 \pm 9) \text{ keV} \cdot (0.56/\text{BR}_{f_2\pi})$.

4 Conclusions

We have measured the radiative widths of the $a_2(1320)$ and $\pi_2(1670)$ resonances produced in pion-nucleus interactions via the Primakoff mechanism using a partial-wave analysis for a clean identification of the two states. The value for the $a_2(1320)$ is $\Gamma_0(a_2(1320) \rightarrow \pi\gamma) = (358 \pm 6 \pm 42) \text{ keV}$. Comparing our measurement with theoretical predictions, we find our result consistent with the calculation from the VMD model given in ref. [1], while predictions from quark models are substantially lower. For the first time we present a value for the radiative width of the $\pi_2(1670)$, $\Gamma_0(\pi_2(1670) \rightarrow \pi\gamma) = (181 \pm 11 \pm 27) \text{ keV} \cdot (0.56/\text{BR}_{f_2\pi})$. This is the first observation of the radiative width of an $E2$ transition in meson spectroscopy, which may provide constraints for further model calculations.

We gratefully acknowledge the support of the CERN management and staff and the skill and effort of the technicians of our collaborating institutes. Special thanks go to V. Pesaro for his technical support during the installation and the running of this experiment. This work was made possible by the financial support of our funding agencies. We would like to thank Prof. N. Kaiser (TUM) for his helpful comments.

Appendix A.

Appendix A.1. The extended maximum-likelihood fit

The physics interpretation of the experimental data is developed in terms of simple models based on eq. (6). Within these models, the transition amplitudes T_{ir}^ϵ have to be optimised individually for each mass bin Δm_{fit} such that the best possible agreement of $\Delta\sigma_m(\tau, t')$ with the distribution of the experimental data in the respective mass bin is achieved. This is realized by using the extended likelihood method to maximise the following expression for every mass bin Δm :

$$\begin{aligned} \ln \mathcal{L} &= \sum_{n=1}^{N_{\text{events}}} \ln \Delta\sigma_{m_n}(\tau_n, t'_n) \\ &\quad - \underbrace{\int \Delta\sigma_m(\tau, t') \eta(\tau, m, t') d\Phi(\tau) dm dt'}_{=N_{\text{events for the converged fit}}} \\ &= \sum_{n=1}^{N_{\text{events}}} \ln \left[\sum_{\epsilon, r} \sum_{ij} T_{ir}^\epsilon T_{jr}^{\epsilon*} \right. \\ &\quad \left. \bar{f}_i^\epsilon(t'_n, m_n) \bar{\psi}_i^\epsilon(\tau_n, m_n) \bar{f}_j^{\epsilon*}(t'_n, m_n) \bar{\psi}_j^{\epsilon*}(\tau_n, m_n) \right] \\ &\quad - \sum_{\epsilon, r} \sum_{ij} T_{ir}^\epsilon T_{jr}^{\epsilon*} I_{ij}^\epsilon. \end{aligned} \quad (\text{A.1})$$

The pre-calculated normalisation integrals are given by

$$\begin{aligned} I_{ij}^\epsilon &= \int \bar{f}_i^\epsilon(t', m) \bar{\psi}_i^\epsilon(\tau, m) \bar{f}_j^{\epsilon*}(t', m) \bar{\psi}_j^{\epsilon*}(\tau, m) \\ &\quad \times \eta(\tau, m, t') d\Phi(\tau) dm dt'. \end{aligned} \quad (\text{A.2})$$

For pairs of individual amplitudes i and j , the integration is performed over the phase space τ , the three-pion mass m inside Δm_{fit} , and the t' range used in this analysis. The expression $f_i^\epsilon(t, m) \psi_i^\epsilon(\tau, m)$ is evaluated using phase-space Monte Carlo events. Their number exceeds the experimental number of events by typically a factor 5–10, such that their statistical uncertainty can be neglected. The factor $\eta(\tau, m, t')$ takes into account the acceptance of the spectrometer. Note that the integral in eq. (A.2) is normalised such that if $\eta(\tau, m, t') = 1$ then $I_{ij} = 1$ for $i = j$, and $I_{ij} = 0$ for $i \neq j$. With this normalisation the fitted number $\sum_r T_{ir}^\epsilon T_{jr}^{\epsilon*}$ refers to the number of events in a partial wave i , cf. eq. (9).

The fitting procedure is carried out for each mass bin individually, with typically 10–50 independent fit attempts with random starting values of the parameters per mass bin until the best fit yields optimized sets of T_{ir}^ϵ with their statistical uncertainties.

Appendix A.2. The concept of partial coherence

Incoherence effects may be observed in a PWA of experimental data, even if a coherent production process takes place. In the data presented in this paper, these effects are related to the resolution effects discussed in sect. 2.2. In these cases, using $N_r > 1$ in eq. (6) often allows for too much freedom between the production amplitudes T_{ir}^ϵ that appear N_r times in the PWA fit. Instead, the observed incoherence can be taken into account by using partial coherences. This allows limited coherence between selected sets of decay amplitudes and thus reweighting of individual off-diagonal terms in the coherent sum, as illustrated by:

$$\sum_{ij} T_i T_j^* \psi_i \psi_j^* \rightarrow \sum_{ij} r_{ij} T_i T_j^* \psi_i \psi_j^*. \quad (\text{A.3})$$

Here, $r_{ij} \leq 1$ are real numbers that reflect the reduction of coherence between the decay amplitudes i and j , with $r_{ij} = r_{ji}$. They decrease the contribution of the interference of the amplitudes i and j , without introducing additional phases as $N_r > 1$ does. These parameters are usually also fitted. The intensities of the individual decay amplitudes are preserved by fixing $r_{ii} \equiv 1$.

Appendix A.3. Parameterisation of the ChPT amplitude

The transition amplitude \mathcal{A} of a process contributing to the reaction $\pi^- \gamma \rightarrow \pi^- \pi^- \pi^+$ has the general form

$$\mathcal{A} = \frac{2e}{m_\pi^2} (\boldsymbol{\epsilon} \cdot \mathbf{q}_1 A_1 + \boldsymbol{\epsilon} \cdot \mathbf{q}_2 A_2). \quad (\text{A.4})$$

Here \mathbf{q}_1 and \mathbf{q}_2 are the three-momenta of the two outgoing π^- in the Gottfried-Jackson reference system, which are complemented with \mathbf{q}_3 and \mathbf{p}_1 , the three-momenta of the outgoing π^+ and the incoming π^- , respectively, and $\hat{k} = (0, 0, -1)$, the unit vector of the photon momentum \mathbf{k} . The reference system is determined in the rest frame of the 3π system. Its z -axis is in the direction of the

incoming beam particle, the y -axis perpendicular to the production plane, *i.e.* given by $\mathbf{p}_{\text{recoil}} \times \hat{z}$ with $\mathbf{p}_{\text{recoil}}$ being the three-momentum of the recoil particle, and $\hat{x} = \hat{y} \times \hat{z}$. Equation (A.4) uses the elementary electric charge e , the transverse polarisation vector of the photon $\boldsymbol{\epsilon}$, and the amplitudes A_1 and A_2 that contain the dynamical information. The calculation is performed using the radiation gauge, where $\boldsymbol{\epsilon} \cdot \hat{k} = 0$. When the cross section σ is calculated, the amplitude \mathcal{A} is squared and the average of the transverse polarisation states of the photon is evaluated, which leads to the following square of the vector product:

$$\sigma \propto [(A_1 \mathbf{q}_1 + A_2 \mathbf{q}_2) \times \hat{k}]^2. \quad (\text{A.5})$$

The amplitudes A_1 and A_2 are expressed in terms of the dimensionless Mandelstam variables $s = (p_1 + k)^2/m_\pi^2$, $s_1 = (q_1 + q_3)^2/m_\pi^2$, $s_2 = (q_2 + q_3)^2/m_\pi^2$, $t_1 = (k - q_1)^2/m_\pi^2$ and $t_2 = (k - q_2)^2/m_\pi^2$. The amplitudes A_1 and A_2 transform into each other by the relation $A_2(s, s_1, s_2, t_1, t_2) = A_1(s, s_2, s_1, t_2, t_1)$.

For the implementation into the PWA the amplitude \mathcal{A} is represented in the reflectivity basis. The ChPT amplitude employed in our analysis is implemented as

$$\Psi_{\text{ChPT}}^{\epsilon=+1} = \frac{1}{\sqrt{s-1}} (A_1 q_1[x] + A_2 q_2[x]) \quad (\text{A.6})$$

and

$$\Psi_{\text{ChPT}}^{\epsilon=-1} = \frac{1}{\sqrt{s-1}} (-A_1 q_1[y] - A_2 q_2[y]), \quad (\text{A.7})$$

where $q_i[j]$ is the j -component of the momentum \mathbf{q}_i in the Gottfried-Jackson reference system. The term $1/\sqrt{s-1}$ originates from the flux factor in the cross section.

The ChPT amplitude employed in the presented PWA takes into account the tree-level calculation given in ref. [16], the calculation of loops and the necessary counterterms from ref. [17], and also ρ -exchange contributions. The ρ -exchange contribution to A_1 of eqs. (A.6) and (A.7), which were provided by ref. [23], are explicitly written down as

$$\begin{aligned} A_1^\rho = & \frac{g_{\rho\pi}^2}{b^2(3-s-t_1-t_2)} \\ & \times \left[\frac{(2s+1-2s_2-s_1+t_1)(s-2-s_1+t_2)^2}{b+s-2-s_1+t_2-\Sigma_\rho(2-s+s_1-t_2)} \right. \\ & + \left. \frac{(2s+1-2s_1-s_2+t_2)(s-2-s_2+t_1)^2}{b+s-2-s_2+t_1-\Sigma_\rho(2-s+s_2-t_1)} \right] \\ & + \frac{g_{\rho\pi}^2}{b^2(t_1-1)} \left[\frac{(2s-2s_1-s_2+t_1+2t_2-1)s_2^2}{b-s_2-\Sigma_\rho(s_2)} \right. \\ & + \left. \frac{(s+1-s_1-2s_2+t_1+t_2)(s-2-s_1+t_2)^2}{b+s-2-s_1+t_2-\Sigma_\rho(2-s+s_1-t_2)} \right] \\ & + \frac{g_{\rho\pi}^2}{b^2} \left[\frac{s_2(1-s_2-t_2)}{b-s_2-\Sigma_\rho(s_2)} + \frac{s_1(s-2-2s_1+t_2)}{b-s_1-\Sigma_\rho(s_1)} \right. \\ & + \left. \frac{(s_2+1-t_1)(s-2-s_2+t_1)}{b+s-2-s_2+t_1-\Sigma_\rho(2-s+s_2-t_1)} \right]. \end{aligned} \quad (\text{A.8})$$

Table 4. The set of decay amplitudes used for the PWA fit for the extraction of the intensities of $a_2(1320)$ and $\pi_2(1670)$.

$J^{PC} M^\epsilon$	L	{Isobar} π	Thr. [GeV]
0^-+0^+	S	$(\pi\pi)_s\pi$	–
0^-+0^+	S	$f_0(980)\pi$	1.12
0^-+0^+	P	$\rho\pi$	–
0^-+0^+	D	$f_2\pi$	1.24
0^-+0^+	S	$f_0(1500)\pi$	1.64
$1^{++}0^+$	S	$\rho\pi$	0.48
$1^{++}0^+$	P	$f_2\pi$	1.40
$1^{++}0^+$	P	$f_0(980)\pi$	1.24
$1^{++}0^+$	P	$(\pi\pi)_s\pi$	–
$1^{++}0^+$	D	$\rho\pi$	1.04
$1^{++}1^+$	S	$\rho\pi$	0.76
$1^{++}1^+$	P	$(\pi\pi)_s\pi$	0.92
1^-+1^+	P	$\rho\pi$	1.48
$2^{++}1^+$	D	$\rho\pi$	0.92
2^-+0^+	S	$f_2\pi$	1.24
2^-+0^+	P	$\rho\pi$	0.80
2^-+0^+	D	$(\pi\pi)_s\pi$	1.32
2^-+0^+	D	$f_2\pi$	1.52
2^-+0^+	F	$\rho\pi$	1.28
2^-+1^+	S	$f_2\pi$	1.38
2^-+1^+	P	$\rho\pi$	1.28
2^-+1^+	D	$(\pi\pi)_s\pi$	1.24
2^-+1^+	F	$\rho\pi$	1.52
$3^{++}0^+$	P	$f_2\pi$	1.52
$3^{++}0^+$	D	$\rho\pi$	1.52
ChPT trees+loops+rho $\epsilon = +1$			< 1.56
$1^{++}1^-$	S	$\rho\pi$	0.76
$1^{++}1^-$	P	$(\pi\pi)_s\pi$	0.92
1^-+1^-	P	$\rho\pi$	1.48
$2^{++}1^-$	D	$\rho\pi$	0.92
2^-+1^-	S	$f_2\pi$	1.36
2^-+1^-	P	$\rho\pi$	1.28
2^-+1^-	D	$(\pi\pi)_s\pi$	1.24
2^-+1^-	F	$\rho\pi$	1.52
ChPT trees+loops+rho $\epsilon = -1$			< 1.56
Kaon decay			< 0.56
Background			–

Table 5. Parameters used in eq. (A.12) to describe the mass dependence of decay amplitudes in the $\pi_2(1670)$ mass region considered in the analysis described in sect. 2.3.

Amplitude(s) $J^{PC} M^\epsilon \{\text{isobar}\} [L]\pi$	m_j [GeV/c ²]	Γ_j [GeV/c ²]	α_j [(GeV/c ²) ⁻¹]	$p_{4,j}$	$p_{5,j}$	$p_{6,j}$
$0^-+0^+(\pi\pi)_S[S]\pi$	1.8188	0.23117	4.5104	43.180	12512.0	-43305.0
$0^-+0^+f_0(980)[S]\pi$	1.8094	0.23515	-0.36871	28.042	3.0863	-0.57855
$0^-+0^+\rho[P]\pi$	1.5150	0.20004	1.1676	47.787	43.133	-162.45
$1^{++}0^+\rho[S]\pi$	1.3051	0.31616	7.3830	101.58	238700.0	23925.0
$1^{++}0^+\rho[D]\pi$	1.5943	0.26680	1.5255	53.629	-77.010	-524.38
$1^{++}0^+(\pi\pi)_S[P]\pi$	1.3763	0.74318	0.49296	89.914	76.893	-17.233
$1^{++}0^+f_2(1270)[P]\pi$	1.6815	0.25355	1.3663	34.721	-33.388	-232.13
$2^-+0^+f_2(1270)[S]\pi$ $2^-+0^+\rho[P/F]\pi$ $2^-+1^\pm f_2(1270)[S]\pi$ $2^-+1^\pm\rho[P/F]\pi$	1.672	0.260	-	-	-	-
$2^-+0^+f_2(1270)[D]\pi$	1.7782	0.24392	3.1200	18.036	-1756.3	-284.26

This notation uses the coupling constant $g_{\rho\pi} = 6.03$ and the squared mass ratio $b = (m_\rho/m_\pi)^2 = 30.4367$. The energy-dependent self-energy Σ_ρ of the ρ is given by

$$\text{Im } \Sigma_\rho(x) = \frac{g_{\rho\pi}^2}{48\pi\sqrt{x}}(x-4)^{3/2}\theta(x-4), \quad (\text{A.9})$$

where $\text{Im } \Sigma_\rho(x=b) = m_\rho\Gamma_\rho$ with $\Gamma_\rho = 150$ MeV, and

$$\begin{aligned} \text{Re } \Sigma_\rho(x) = & \frac{g_{\rho\pi}^2}{24\pi^2}x \left[\frac{4}{b} - \frac{4}{x} \right. \\ & - \left(1 - \frac{4}{x}\right)^{3/2} \ln\left(0.5\left(\sqrt{|x|} + \sqrt{|x-4|}\right)\right) \\ & \left. + \left(1 - \frac{4}{b}\right)^{3/2} \ln\left(0.5\left(\sqrt{b} + \sqrt{b-4}\right)\right) \right]. \end{aligned} \quad (\text{A.10})$$

Terms like $\Sigma_\rho(s_{1,2})$ in eq. (A.8) refer to contributions from real ρ , which decay into $\pi^+\pi^-$ pairs so that $s_{1,2} > 4$, and are complex-valued. In case of a virtual ρ , where the ρ -exchange mediates the $\pi\pi$ -interaction, the self-energy reads like $\Sigma_\rho(2-s+s_{1,2}-t_{2,1})$, with $2-s+s_{1,2}-t_{2,1} < 0$, and is purely real-valued.

Appendix A.4. Set of decay amplitudes

Table 4 shows the set of decay amplitudes used for the PWA presented in this paper. The wave set includes established amplitudes with $M^\epsilon = 0^+$ attributed to diffractive dissociation. The amplitudes related to Primakoff production are provided as isobaric $M = 1$ amplitudes or as

the ChPT amplitude. All Primakoff amplitudes are introduced with both $\epsilon = \pm 1$ which is necessary due to the limited resolution as explained in sect. 2.2. Also included in the fit are an amplitude describing the decay of beam kaons into $\pi^-\pi^-\pi^+$, and an incoherent background wave that is homogeneous in phase space. Many amplitudes are introduced with an upper or lower threshold which is chosen in order to constrain them to the region where they are expected to contribute.

Appendix A.5. Parameterisation of the decay amplitudes for the PWA covering the mass region of the $\pi_2(1670)$ in bins of t'

For the PWA fit covering the mass region around the $\pi_2(1670)$, *i.e.* $1.50 \text{ GeV}/c^2 < m_{3\pi} < 1.80 \text{ GeV}/c^2$, in small bins of t' (see sect. 2.3), both mass dependences and phases have to be taken into account. The resonances are parameterised by Breit-Wigners functions, and the background by exponentials in $m_{3\pi}$. As the background to the amplitudes can stem from tails of higher-mass resonances, it is added coherently with a mass-dependent relative phase. Breit-Wigner functions and background distributions are summed to single complex-valued terms, denoted in the following by $B_j(m)$. Their parameters were obtained by fitting the square of these $B_j(m)$ to the respective intensity of each amplitude. These terms are then multiplied by the normalised decay amplitudes, *i.e.* in every t' bin the PWA uses the following decay amplitudes:

$$\overline{\psi}_j(\tau, m) = \frac{\psi_j(\tau)B_j(m)}{\sqrt{\int |\psi_j(\tau)|d\Phi(\tau)}}, \quad (\text{A.11})$$

with

$$B_j(m) = p_{4,j} \frac{\sqrt{m_j \Gamma_j}}{m_j^2 - m^2 - i m_j \Gamma_j} + p_{5,j} \exp(-\alpha_j m) + i p_{6,j} \exp(-\alpha_j m). \quad (\text{A.12})$$

Here, m_j is the nominal mass, Γ_j is the nominal width of the resonance, α_j describes the background, and $p_{4,j}$, $p_{5,j}$, and $p_{6,j}$ are adjusted to the relative strengths of Breit-Wigner and background contributions. This background is disregarded for the $J^{PC} = 2^{-+}$ amplitudes that contain the $\pi_2(1670)$, as satisfactory fits were obtained without this background, thus avoiding artificial phase shifts in the resonance region. An exception is the $2^{-+}0^+ f_2[D]\pi$ amplitude that seems rather to contain the higher-mass $\pi_2(1880)$, which is not further discussed here. All used parameters are derived from fits to intensities in small mass bins, and given in table 5. The mass dependences of all waves of minor strength, not included in table 5 but used in the PWA fit, are described by a polynomial behaviour,

$$B_j(m) = \sqrt{0.19746 - 0.32710 m + 0.18933 m^2 - 0.037275 m^3}, \quad (\text{A.13})$$

instead of using eq. (A.12).

References

1. J.L. Rosner, Phys. Rev. D **23**, 1127 (1981).
2. I.G. Aznauryan, K.A. Oganessian, Sov. J. Nucl. Phys. **47**, 1097 (1988).
3. S. Ishida, K. Yamada, M. Oda, Phys. Rev. D **40**, 1497 (1989).
4. T. Maeda, K. Yamada, M. Oda, S. Ishida, to be published in Prog. Theor. Exp. Phys, arXiv:1013.7507 [hep-ph].
5. I.Ya. Pomeranchuk, I.M. Shmushkevich, Nucl. Phys. **23**, 452 (1961).
6. Particle Data Group (J. Beringer *et al.*), Phys. Rev. D **86**, 010001 (2012).
7. G. Fäldt, Ulla Tengblad, Phys. Rev. C **79**, 014607 (2009).
8. G. Fäldt, Ulla Tengblad, Phys. Rev. C **87**, 029903 (2013).
9. G. Fäldt, Phys. Rev. C **82**, 037603 (2010).
10. The COMPASS Collaboration (P. Abbon *et al.*), Nucl. Instrum. Methods A **577**, 455 (2007).
11. The COMPASS Collaboration (C. Adolph *et al.*), Phys. Rev. Lett. **108**, 192001 (2012).
12. K. Gottfried, J. Jackson, Nuovo Cimento **33**, 309 (1964).
13. J.D. Hansen *et al.*, Nucl. Phys. B **81**, 403 (1974).
14. S.U. Chung, Phys. Rev. D **56**, 7299 (1997).
15. M. Perl, *High Energy Hadron Physics* (Wiley-Interscience, New York, 1974).
16. N. Kaiser, J.M. Friedrich, Eur. Phys. J. A **36**, 181 (2008).
17. N. Kaiser, Nucl. Phys. A **848**, 198 (2010).
18. F.V. Hippel, C. Quigg, Phys. Rev. D **5**, 624 (1972).
19. M.G. Bowler, Phys. Lett. B **182**, 400 (1986).
20. J. Pisut, M. Roos, Nucl. Phys. B **6**, 325 (1968).
21. V.V. Molchanov *et al.*, Phys. Lett. B **521**, 171 (2001).
22. S.U. Chung, J.M. Friedrich, Phys. Rev. D **78**, 074027 (2008).
23. N. Kaiser, private communication (2011–2013).
24. S. Cihangir *et al.*, Phys. Lett. B **117**, 119 (1982).
25. E.N. May *et al.*, Phys. Rev. D **16**, 1983 (1977).